


## Dynamics and control of separated flow over small-scale surface deformations with slip

Silvia Ceccacci 

*Barcelona Supercomputing Center (BSC-CNS), CASE Department, 08034 Barcelona, Spain*

Sophie A. W. Calabretto 

*School of Engineering, University of Leicester, Leicester LE1 7RH, United Kingdom*

Christian Thomas \*

*School of Mathematical and Physical Sciences, Macquarie University, NSW 2109, Australia*

James P. Denier 

*St Ives, Sydney, NSW 2075, Australia*



(Received 6 September 2023; accepted 26 February 2024; published 12 March 2024)

Surface slip was employed to control flow separation induced by small-scale Gaussian-shaped surface deformations on a two-dimensional flat plate. Single-surface deformations, including bumps and gaps, were modeled, which generated separated flow along the rear side of the bump and within the gap concavity for a Reynolds number  $Re = 100\,000$  when the plate surface was subject to the no-slip condition. Surface slip was modeled using a Navier-slip condition and quantified by a slip length  $\lambda$ . Bump deformations had a greater impact on the flow dynamics than gap concavities, generating more intense regions of reversed flow and requiring larger slip lengths to inhibit flow separation. In addition, double-bump configurations were modeled, with the location of the two bumps playing a critical role in the evolution of the flow. When the bumps were close together, the first bump controlled the size of the separation bubble that developed downstream of the second bump. Whereas when bumps were far apart, a moderate slip length  $\lambda$  excited nonlinear oscillatory flow. However, increasing the slip length suppressed this phenomenon and ultimately eliminated all pockets of separated flow.

DOI: [10.1103/PhysRevFluids.9.033902](https://doi.org/10.1103/PhysRevFluids.9.033902)

### I. INTRODUCTION

Laminar flow separation occurs in many engineering applications, such as aerodynamics and turbomachinery. An adverse pressure gradient induces flow separation and usually results in a performance loss. For example, geometrical alterations to a surface, such as a smooth bump mounted on a flat plate, may trigger flow separation [1–3]. In this geometrical configuration, the flow transitions from a favorable to an adverse pressure gradient along the rear side of the bump, which can establish unstable behavior, including convective and absolute instabilities. Convective instabilities emerge when a disturbance forms a wave packet in the spatiotemporal plane that propagates away from the initial source, and absolute instability develops if the disturbance grows in time at every spatial position and eventually spreads across the entire spatiotemporal domain.

---

\*christian.thomas@mq.edu.au

Further details on instabilities in spatially developing flows can be found in Huerre and Monkewitz [4] and Chomaz [5].

Marquillie and Ehrenstein [1] numerically investigated the stability of separated flow behind a two-dimensional bump on an otherwise flat plate and observed nonlinear oscillations, otherwise known as low-frequency flapping. The loss of stability of this separated flow is associated with a set of localized modes becoming simultaneously unstable [2]. Passaggia *et al.* [3] undertook an experimental study and gave evidence of low-frequency flapping and transverse instability, thus confirming the numerical observations. In fact, for a Reynolds number  $Re > 500$  (based on the displacement thickness), rapid oscillations developed similar to noise dynamics brought about by the Kelvin-Helmholtz instability. While at  $Re \approx 590$ , global, low-frequency oscillations of the recirculation bubble emerge. Passaggia and Ehrenstein [6] studied a control method from the fully developed nonlinear flapping state back to the steady state using a single actuator. The method is based on the decomposition between the slow dynamics of the base flow modification, and the fast dynamics (i.e., flapping) of the globally unstable two-dimensional separated boundary layer over the bump.

Several control methods for separated flows have been tested [7,8]. These include, for example, superhydrophobic surfaces or coatings that alter the surface texture [9–12]. Following recent developments in nanotechnology and laser physics, it is now feasible to thermally modify surface architecture and chemistry to attain superhydrophobicity [13]. Superhydrophobic surfaces (or coatings) provide significant beneficial control effects, including drag reduction in marine vessels [14,15]. Further reviews of superhydrophobic surfaces for drag reduction are given by Rothstein [16] and Golovin *et al.* [17].

The multifunctional properties of superhydrophobic coatings, such as antifogging, oil-water separation, anti-icing, self-cleaning, and antibacterial, make them applicable in many other fields [13]. The most predominantly used materials to fabricate superhydrophobic surfaces are metal oxides due to their adaptability with most fabrication techniques, low cost, and environmentally friendly properties [13,18]. However, these surfaces lack mechanical robustness. This issue is addressed by introducing hierarchical roughness structures to reduce damage to the surface features [19].

The potential for superhydrophobic surfaces to be manufactured and used within different contexts has made them a mechanism for flow control and drag reduction. In the numerical context, superhydrophobic surfaces are often modeled using slip boundary conditions. The low-viscosity fluid acts as a lubricating layer, which allows the flow to slip over the surface [11]. The slip velocity offsets the shear strain rate and thus reduces the wall friction. Aside from the slippage effect, the pressure coupling effect between a superhydrophobic surface and a turbulent boundary layer was investigated by Seo *et al.* [20]. The surface texture provides an additional mechanism for flow control, such as riblets and grooves [21,22], especially when oriented in the streamwise direction [23,24]. These are also referred to as drag-altering textured surfaces [25], which have been proven to reduce skin-friction drag [26] and influence laminar-turbulent transition processes [27].

In this paper, flow separation is generated by a geometrical alteration of the two-dimensional flat plate that takes the form of either a small-scale Gaussian-shaped bump or gap, similar to that investigated by Marquillie and Ehrenstein [1], Ehrenstein and Gallaire [2], Passaggia *et al.* [3], Mollicone *et al.* [28], and Ceccacci *et al.* [29]. The Reynolds number of the flow [defined below in Eq. (2)] and the dimensions of the surface deformations are chosen to be sufficiently large to establish pockets of separated flow. Similar flow features to those described by the above authors are recovered in the instance the surface is subject to no-slip boundary conditions: the flow transitions from a favorable to an adverse pressure gradient, leading to flow separation along the rear side of the bump or within the gap concavity. In addition to single-bump arrangements, double-bump configurations are modeled that establish multiple regions of separated flow. A slip boundary condition is applied to the plate to convey a quality of roughness to the deformed surface,

the aim being to ascertain the effect of slip on the development of flow separation. Ceccacci *et al.* [29] recently undertook a similar numerical study but for bump deformations in a two-dimensional channel. Applying a slip condition to the surface deformity was found to inhibit flow separation along the rear side of the bump. Motivated by the observations of Ceccacci and coworkers, we wish to determine if a slip surface brings about comparable favorable control benefits to other geometries, in particular, the boundary layer that develops over a deformed two-dimensional flat plate. And if so, what level of slip is necessary to suppress pockets of separated flow, and how do the requirements differ for bump and gap deformations? Moreover, what is the effect on the flow dynamics for multiple deformation configurations?

Niavarani and Priezjev [30] defined the effective slip length with respect to the level of the mean height of the surface roughness. This choice was motivated by the study of molecular dynamics, which demonstrates that the effective slip length in a flow of simple fluids [31] agrees with hydrodynamic predictions when the corrugation wavelength exceeds approximately 30 molecular diameters [30]. The type of roughness varies and includes, for instance, uniform sand grains [32] and sandpaper [33]. In general, for each new roughness geometry, it is necessary to determine the effective roughness height and the virtual origin of the boundary layer. Ibrahim *et al.* [25] have undertaken steps towards a virtual-origin unifying framework for drag-altering surfaces. The framework holds for the case where imposed virtual origins remain relatively small compared to the characteristic length scales of the near-wall turbulence. Thus far, due to different design configurations and flow conditions, universal criteria for surface roughness that convey beneficial conclusions on flow control are inconsistent [34,35]. For this reason, research efforts are ongoing to uncover surface parameters (including the slip length) that lead to frictional drag reduction and flow control benefits.

In the following investigation, surface slip is modeled using a spatially homogeneous Navier (Robin) slip boundary condition [36]

$$u_{\parallel} = g(x, \lambda) \frac{\partial u_{\parallel}}{\partial n} \quad \text{and} \quad u_{\perp} = 0,$$

where  $u_{\parallel}$  and  $u_{\perp}$  represent the respective tangential and wall-normal velocities over the surface [37,38]. The function  $g(x, \lambda)$  models slip across the length of the flat plate and surface deformations, while  $n$  denotes the normal to the wall. The tangential velocity on the boundary  $u_{\parallel}$  is the slip velocity and is linked to the mean wall shear by the slip length  $\lambda$ . This boundary condition was used to predict the performance of superhydrophobic surfaces in several earlier studies [37,39]. In laminar flows (where drag reduction is described by the streamwise slip length), a streamwise slip condition increases the mean velocity and establishes a drag reduction [40]. A Robin-type Navier slip condition, as applied in this study, can be used to model flows over surfaces with a modification in the flat reference surface, such as those induced by roughness, riblets, or other drag reduction devices, for which a slip length can be retrieved [41]. Pralits *et al.* [42] used a Navier slip condition to represent, in a homogenized sense, the alternation of no-slip and no-shear elongated regions due to microridges covering walls. The assumption is that the gas within the cavities does not impose any shear stress on the liquid above. For surfaces featuring roughness or riblets, the slip length can be related to the protrusion height [43–45]. The protrusion height is defined as the distance between the rib tip and the average origin of the velocity profile near the surface. Luchini *et al.* [45] expanded on this concept and identified two distinct heights, the longitudinal and transverse protrusion heights, which are associated with the flow along the length and across the surface. Their investigation emphasized that the meaningful quantity lies in the difference between these two heights.

This paper is organized as follows. In Sec. II, the mathematical formulation of the problem is outlined; in Sec. III, the computational details regarding the direct numerical simulations (DNS) performed are described; in Sec. IV, the results obtained for single, isolated surface deformations are presented; in Sec. V, the results obtained for double-bump configurations are shown; finally, in Sec. VI, concluding remarks are made.

## II. MODEL

### A. Navier-Stokes equations and Blasius flow

Consider a two-dimensional, incompressible fluid with kinematic viscosity  $\nu^*$  and density  $\rho^*$  flowing over a semi-infinite flat plate. The direction normal to the plate is denoted  $y^*$ , while  $x^*$  measures the streamwise distance along the plate. (Here an asterisk denotes dimensional quantities.) On nondimensionalizing Cartesian coordinates  $(x^*, y^*)$  by the reference length scale  $L^*$ , velocities  $\mathbf{u}^* = (u^*, v^*)$  by the free-stream velocity  $U_\infty^*$ , and pressure  $p^*$  by  $\rho^* U_\infty^{*2}$ , the nondimensional incompressible Navier-Stokes equations in Cartesian coordinates are given as

$$\frac{\partial \mathbf{u}}{\partial t} + (\mathbf{u} \cdot \nabla) \mathbf{u} = -\nabla p + \frac{1}{\text{Re}} \nabla^2 \mathbf{u}, \quad (1a)$$

$$\nabla \cdot \mathbf{u} = 0, \quad (1b)$$

where the Reynolds number

$$\text{Re} = \frac{U_\infty^* L^*}{\nu^*}. \quad (2)$$

In the subsequent investigation  $\text{Re} = 100\,000$ , which is sufficiently large to establish pockets of separated flow near the surface deformations modeled along the length of the flat plate.

In the absence of surface deformations, the flow over the flat plate is described by the Blasius boundary layer. Assuming a zero-pressure gradient along the  $x$  direction (that is,  $\partial p / \partial x = 0$ ) and large Reynolds number  $\text{Re}$ , the velocity  $\mathbf{u}$  is obtained by solving the Blasius equation

$$f''' + \frac{1}{2} f f'' = 0, \quad (3)$$

where  $f = f(z)$  is the Blasius similarity solution for the similarity variable  $z = y^* / \delta^*$ , and boundary layer thickness  $\delta^* = \sqrt{\nu^* x^* / U_\infty^*}$  [46]. Equation (3) is solved subject to the boundary conditions

$$f(0) = f'(0) = 0 \quad \text{and} \quad f'(z \rightarrow \infty) = 1, \quad (4a,b)$$

where a prime denotes differentiation with respect to  $z$ . The dimensional streamwise  $u^*$  and wall-normal  $v^*$  velocity profiles are given by

$$u^* = U_\infty^* f' \quad \text{and} \quad v^* = \frac{1}{2} \sqrt{\frac{\nu^* U_\infty^*}{x^*}} (z f' - f), \quad (5a,b)$$

respectively.

### B. Surface deformations

Along the flat plate, two-dimensional Gaussian-shaped surface deformations are modeled using the coordinate transformation

$$(x, y) = (\bar{x}, g(\bar{x}, \bar{y})), \quad (6a)$$

where the function  $g(\bar{x}, \bar{y})$  maps the computational coordinates  $(\bar{x}, \bar{y})$  onto the Cartesian coordinates  $(x, y)$  [47]. The mapping function

$$g(\bar{x}, \bar{y}) = \bar{y} \pm h e^{-(\bar{x}-x_c)^2 / (2\sigma^2)} \frac{\tanh(0.1 - \bar{y})}{\tanh(0.1)} \quad (6b)$$

establishes a Gaussian-shaped bump (or gap), centered about  $x_c$  ( $\equiv x_c^* / L^*$ ), of height (or depth)  $h$  ( $\equiv h^* / L^*$ ), and width  $\sigma$  ( $\equiv \sigma^* / L^*$ ). A bump forms for  $h > 0$ , while  $h < 0$  corresponds to a surface indentation. The aspect ratio of the deformation is defined as  $\eta = h / \sigma$ . Similar to the description of the height  $h$ ,  $\eta > 0$  establishes bumps and  $\eta < 0$  gaps. The  $\bar{y}$ -dependent hyperbolic tangent function is included in the mapping function (6b) to ensure a suitable transformation of the mesh in the  $(x, y)$  plane.

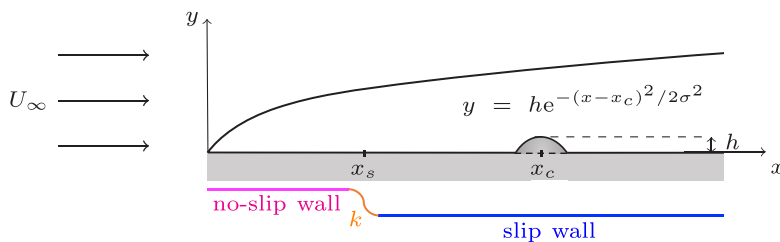


FIG. 1. Diagram of the flow over a flat plate with slip applied to a Gaussian-shaped bump.

The local Reynolds number about the center  $x_c$  ( $\equiv x_c^*/L^*$ ) of the surface deformation is given as

$$\text{Re}_{\delta_c^*} = \frac{U_\infty^* \delta_c^*}{\nu^*} \equiv \sqrt{x_c \text{Re}} \quad (7)$$

for the boundary-layer thickness

$$\delta_c^* = \sqrt{\frac{\nu^* x_c^*}{U_\infty^*}}. \quad (8)$$

Unless otherwise specified, slip effects are investigated for surface deformations centered about the streamwise location  $x_c = 9$ , corresponding to  $\text{Re}_{\delta_c^*} = 948.68$ .

### C. Surface slip

For an impermeable, no-slip surface and suitable geometrical and flow conditions (i.e., dimensions of the surface deformation and Reynolds number  $\text{Re}$ ), the flow separates near the surface deformation. Our model considers the application of a slip condition to the surface deformation as a method of controlling flow separation.

Surface slip is implemented by imposing a linear Robin-type slip condition coupled with the no penetration condition

$$u_{\parallel} - \lambda(x) \frac{\partial u_{\parallel}}{\partial n} = 0 \quad \text{and} \quad u_{\perp} = 0, \quad (9a,b)$$

where  $n$  denotes the direction normal to the wall, and  $u_{\parallel}$  and  $u_{\perp}$  represent the tangential and wall-normal velocities, respectively. The function

$$\Lambda(x) = \frac{\lambda}{1 + e^{-2k(x-x_s)}} \quad (10)$$

prescribes the level of slip along the length of the plate for an effective slip length  $\lambda$  ( $\equiv \lambda^*/L^*$ ). Surface slip is modeled in this way to avoid abrupt changes in the boundary conditions and ensure the wall transitions smoothly from no-slip

$$u_{\parallel} = u_{\perp} = 0 \quad (11a,b)$$

to slip (9) about the streamwise location  $x_s$  ( $\equiv x_s^*/L^*$ ). The parameter  $k$  specifies the sharpness of the step function (i.e., large  $k$  establishes a sharp transition at  $x_s$ ) and is set as  $k = 100$  for the subsequent study. A schematic diagram of the model is illustrated in Fig. 1.

## III. NUMERICAL METHOD

### A. Computational strategy and numerical configuration

The flow over the deformed flat plate was obtained by DNS of the two-dimensional Navier-Stokes (NS) equation (1), using the spectral- $hp$  element method Nektar++ [48]. Here,  $h$  signifies

TABLE I. Parameters characterizing the shape of the Gaussian-shaped surface deformations:  $h$  the height (or depth),  $\sigma$  the width, and  $\eta = h/\sigma$  the aspect ratio of the bumps and gaps. Rows highlighted in gray correspond to those parameters reported in this study, i.e.,  $\eta_1 = 0.16$  and  $\eta_2 = 0.24$ .

$h$	$\sigma$	$\eta$
0.005	0.1250	0.04
0.005	0.0625	0.08
0.010	0.1250	0.08
0.010	0.0938	0.11
0.010	0.0625	0.16
0.015	0.1250	0.12
0.015	0.0938	0.16
0.015	0.0625	0.24
0.020	0.0625	0.32

the geometric flexibility of the  $h$ -type finite-element technique. On the other hand,  $p$  denotes the resolution properties of the spectral method, utilizing high-degree piecewise polynomials up to the  $p$ th order as basis functions. Thus, the spectral- $hp$  element method combines the precision and fast convergence benefits of the spectral element method with the capability of the classical  $h$ -type finite-element method to effectively capture complex geometries and flow behavior.

In addition to the slip condition (9), initial and inlet boundary conditions were given by the solution of the Blasius equation (3). The in-flow boundary condition was prescribed at the stream-wise location  $x_0 = 5$  (that is,  $x_0 = x_0^*/L^* = 5$ ). In addition, the free-stream velocity  $U_\infty^* = 1$  was specified at the upper boundary of the computational domain using a Neumann boundary condition coupled with a zero-pressure condition:

$$\nabla \mathbf{u} \cdot \mathbf{n} = 0 \quad \text{and} \quad p = 0. \quad (12a,b)$$

Here,  $\mathbf{n}$  represents the unit vector normal to the plate surface. A convectivelike outflow condition was imposed at the outlet for all DNS presented herein [49]. Thus, ensuring the flow convects out of the computational domain, i.e., there were no artificial waves reflecting from the outflow boundary condition. (For details regarding the outflow boundary conditions, see [50].)

The parameters that characterize the surface deformations are specified in Table I. Three  $\sigma$  values were selected to establish Gaussian-shaped imperfections with different widths:  $\sigma_1 = 0.0625$  (narrow),  $\sigma_2 = 3\sigma_1/2 = 0.0938$  (medium), and  $\sigma_3 = 2\sigma_1 = 0.125$  (wide). The main surface deformations modeled in this study, highlighted in gray in Table I, correspond to aspect ratios  $\eta_1 = 0.16$  and  $\eta_2 = 0.24$ . These two cases, which have the same width  $\sigma = \sigma_1$ , but different heights (or depths)  $h$ , were chosen to be representative of the effect of slip on the flow separation dynamics. Aspect ratios  $\eta_1$  and  $\eta_2$  represent small and large surface deformations, respectively, and were chosen along with the Reynolds number  $\text{Re} = 100\,000$  to establish pockets of separated flow of varying dimensions, in the instance no slip was applied to the plate surface. It is worth noting that these bump (gap) specifications are smaller than those modeled in earlier investigations [1–3,6].

The computational domain  $\Omega$  was decomposed as  $\Omega_{\bar{x}} \times \Omega_{\bar{y}} = [5, x_{\max}] \times [0, 0.5]$ . The upper boundary of the computational domain was approximately 50 boundary-layer thicknesses  $\delta_c^*$  above the flat plate. In addition, the streamwise location of the outlet  $x_{\max}$  was carefully chosen for each simulation to ensure results were independent of the grid and domain size. Here,  $x_{\max} \in [10, 13]$  were modeled. For instance, for the small deformations of aspect ratio  $\eta_1$ ,  $\Omega_{\bar{x}} = [5, 10]$ , i.e.,  $x_{\max} = 10$ . The spatial discretization in the computational  $(\bar{x}, \bar{y})$  plane comprises a mesh with 4312 quadrilateral elements, as illustrated in Fig. 2. The mesh incorporates  $N_{\bar{y}} = 15$  nodes nonuniformly distributed along the  $\bar{y}$  direction, 10 of which are in the lower half of the computational domain (i.e.,  $\bar{y} \in [0, 0.25]$ ), such that  $\Delta \bar{y} \approx 0.005$  near the flat plate. Along the  $\bar{x}$  direction,  $N_{\bar{x}} = 309$  nodes

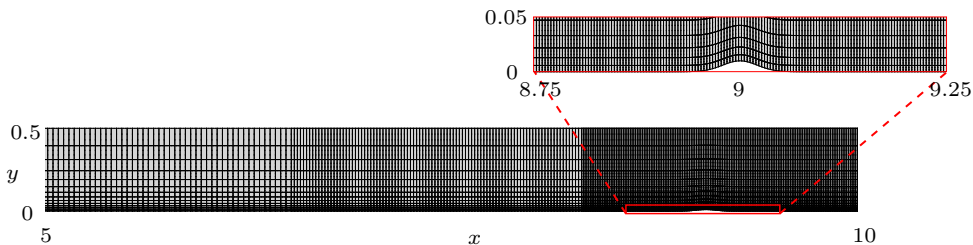


FIG. 2. Mesh used for the single-surface deformations with aspect ratio  $\eta_1 = 0.16$ . The entire computational domain  $\Omega = [5, 10] \times [0, 0.5]$ , and region near the surface deformation centered at  $x_c = 9$ . Diagram not drawn to scale.

were nonuniformly distributed to ensure sufficient grid resolution near the surface deformations. In this region, the grid maintains 24 nodes per  $0.25 \bar{x}$  units of length, i.e.,  $\Delta \bar{x} \approx 0.01$ . For longer computational domains  $\Omega_{\bar{x}}$ , the node density  $N_{\bar{x}}$  was preserved along the  $\bar{x}$  direction to ensure computationally accurate solutions. The same node distribution was applied along the  $\bar{x}$  direction for the large deformations characterized by the aspect ratio  $\eta_2$ , while the number of  $\bar{y}$  nodes was increased to  $N_{\bar{y}} = 22$  with  $\Delta \bar{y} \approx 0.001$  near the flat plate. All meshes were generated using GMSH [51]. Finally, the numerical solution was approximated using eighth-order Lagrange polynomials, and the time integration was performed using a third-order implicit-explicit scheme for a time step  $\Delta t = 2 \times 10^{-5}$ .

The results presented below in Secs. IV and V are shown at time  $t = 20$ , which in most cases was large enough for the flow to have reached a steady state. Like [29], discretization parameters were chosen based on a convergence study, which included a variation of the order of the Lagrange polynomials, mesh size  $N_{\bar{x}}$  and  $N_{\bar{y}}$ , domain length  $\Omega_{\bar{x}}$ , and time step  $\Delta t$ . Percentage errors in the minimum streamwise  $u$  velocity,  $\min(u)$ , were less than 1% and grid independency to within graphical accuracy. Further details are given in Appendixes A and B.

Figure 3 depicts the streamwise  $u$  velocity, with the no-slip boundary condition applied along the plate surface. The solution is shown at time  $t = 20$ , which was sufficient for the flow to attain a steady state. The boundary layer develops from left to right and encounters a small-scale bump

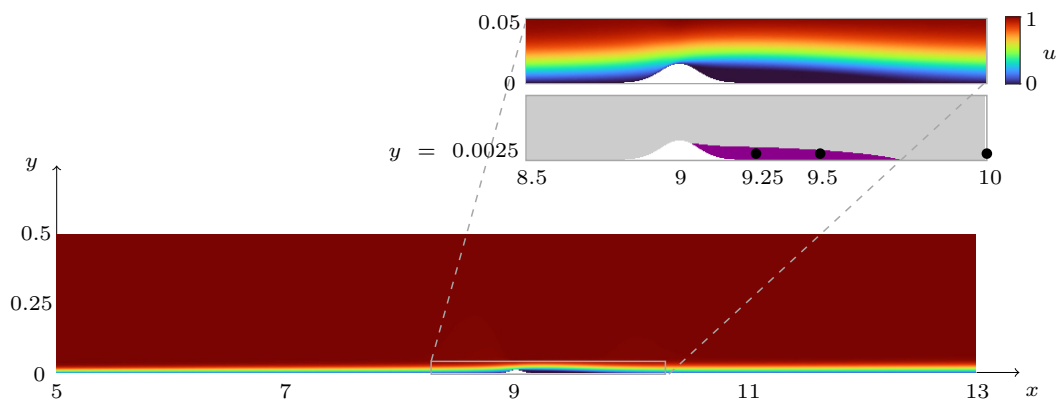


FIG. 3. Illustration of the streamwise  $u$  velocity, at time  $t = 20$ , over a flat plate with a bump centered at  $x_c = 9$  (i.e.,  $\text{Re}_{\delta_*} = 948.68$ ), with aspect ratio  $\eta_2 = 0.24$ . The no-slip boundary condition is applied across the length of the plate, including the bump deformation. The secondary plot highlights the region of flow separation, in purple, where  $u < 0$ . The three black circle markers signify those  $(x, y)$  locations used to trace the temporal evolution of the flow in Fig. 4.



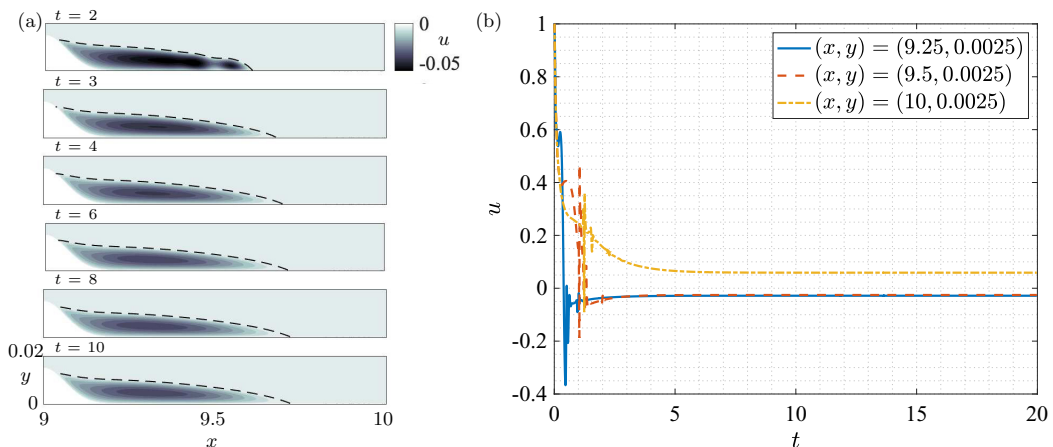


FIG. 4. (a) Contour plots of the streamwise  $u$  velocity in the region of the separated flow downstream of the single-bump configuration in Fig. 3 with aspect ratio  $\eta_2$  and a no-slip wall, at times  $t = 2, 3, 4, 6, 8,$  and  $10$ . Dashed black lines indicate  $u = 0$ . (b) Temporal evolution of the streamwise  $u$  velocity at the three  $(x, y)$  locations identified in Fig. 3 by black circle markers.

at  $x_c = 9$  with aspect ratio  $\eta_2 = 0.24$ . The dimensional height of the bump  $h^* = 0.003 \approx 1.5\delta_c^* \approx 0.3\delta_{99}^*$  at  $x_c = 9$ , where  $\delta_{99}^*$  represents the wall-normal height that the streamwise  $u$  velocity has achieved 99% of the free-stream velocity  $U_\infty^*$ . The flow separates along the rear side of the bump, and following the reattachment of the flow, the boundary layer grows and convects out of the computational domain. Contour levels are plotted for  $u \in [0, 1]$ . Thus, dark red contours represent  $u = 1$ , and the region of reversed flow, corresponding to  $u < 0$ , is represented by dark blue contours, which is further highlighted in a secondary plot by a purple contour.

The evolution of the flow in Fig. 3 from a transient to a steady state, and specifically the separation bubble that forms downstream of the bump, is demonstrated in Fig. 4. Contours of the streamwise  $u$  velocity are plotted in Fig. 4(a) for  $u \in [-0.05, 0]$ , depicting the separated flow along the rear side of the bump. Solutions are plotted at six points in time, from  $t = 2$  through to  $t = 10$ . At time  $t = 2$ , a distinct, elongated pocket of separated flow develops, with a secondary region of recirculating flow emerging about the streamwise position  $x = 9.5$ . As time progresses, the secondary pocket of separated flow dissipates, leaving in its wake a long separation bubble that is relatively unchanged for  $t \geq 4$ . Thus, the flow quickly achieves a steady state. This observation is further confirmed in Fig. 4(b), which illustrates the temporal evolution of the  $u$  velocity at the three  $(x, y)$  locations marked by black circles in Fig. 3. Following a brief transient phase, on the interval  $0 < t < 4$ , the streamwise  $u$  velocity approaches a fixed constant at each location, which is indicative of the flow attaining a steady state. The  $u$  velocity is marginally negative at the two locations within the pocket of separated flow (solid blue and dashed red lines), with a positive value obtained further downstream (chain yellow). In contrast to earlier investigations [1–3,6], the surface bump of aspect ratio  $\eta_2$  does not induce self-sustained oscillatory behavior downstream of the separation bubble, and similarly, for the small bump of aspect ratio  $\eta_1$ . The vortex shedding depicted at time  $t = 2$  in Fig. 4(a) rapidly diminishes, with the flow attaining a steady state. Thus, the dimensions (i.e., height and width) of the two single-bump configurations considered in this study are inadequate for generating the oscillatory phenomena observed in the aforementioned investigations. In Appendix C, a slightly larger bump is modeled that establishes more pronounced vortex shedding and oscillatory behavior at early times  $t$ . However, similar to the behavior illustrated in Fig. 4(a), this dissipates as time increases.



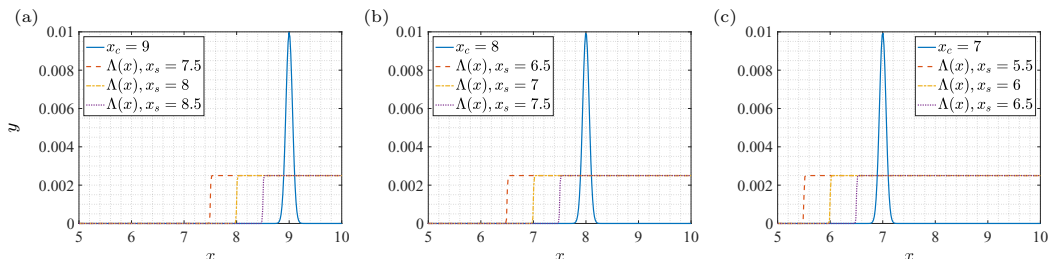


FIG. 5. Plots of a bump deformation with aspect ratio  $\eta_1$  (solid blue lines), centered at (a)  $x_c = 9$ , (b)  $x_c = 8$ , and (c)  $x_c = 7$ . The slip function  $\Lambda(x)$  given by Eq. (10) is plotted with  $x_s$  calculated using Eq. (13), such that  $m = 1.5$  (dashed red),  $m = 1$  (chain yellow), and  $m = 0.5$  (dotted purple). The slip length  $\lambda = 2.5 \times 10^{-3}$ .

### B. Location of $x_s$ with respect to the deformation location $x_c$

The slip function  $\Lambda(x)$ , given by Eq. (10), is governed by the streamwise location  $x_s$  near which the wall condition transitions from no slip to slip. The value of  $x_s$  is informed by testing its influence on the flow dynamics about the location of the surface deformation  $x_c$ . Solid blue lines in Fig. 5 depict three bump deformations with aspect ratio  $\eta_1$ , centered at  $x_c = 9$  (i.e.,  $\text{Re}_{\delta_c^*} = 948.68$ ),  $x_c = 8$  (i.e.,  $\text{Re}_{\delta_c^*} = 894.43$ ), and  $x_c = 7$  (i.e.,  $\text{Re}_{\delta_c^*} = 836.66$ ), respectively. In each instance, three values of  $x_s$  are modeled, with

$$x_s = x_c - m, \quad \text{where } m = 0.5, 1, \text{ and } 1.5. \quad (13)$$

The slip function  $\Lambda(x)$ , with slip length  $\lambda = 2.5 \times 10^{-3}$ , is plotted in each subplot of Fig. 5 for  $x_s = x_c - 1.5$  (dashed red),  $x_s = x_c - 1$  (chain yellow), and  $x_s = x_c - 0.5$  (dotted purple).

The minimum of the streamwise  $u$  velocity,  $\min(u)$ , found within the separation bubble along the rear side of the bump, is reported in Table II for those specifications given in Fig. 5 and slip lengths  $\lambda = 0$ ,  $\lambda = 1.25 \times 10^{-3}$ , and  $\lambda = 2.5 \times 10^{-3}$ . [For the no-slip case  $\lambda = 0$ , the slip function  $\Lambda(x)$  is not required, and  $x_s$  is not specified.] The effect of the location  $x_s$  is negligible. Therefore, for the remainder of this study,  $x_s$  is specified as the furthest point from the deformation center, i.e.,  $m = 1.5$  in Eq. (13). In particular, and unless otherwise specified, the default settings for the subsequent investigation are  $x_c = 9$  and  $x_s = 7.5$ .

TABLE II. Minimum value of the streamwise  $u$  velocity,  $\min(u)$ , for surface deformations with aspect ratio  $\eta_1 = 0.16$ , and slip lengths  $\lambda = 0$ ,  $\lambda = 1.25 \times 10^{-3}$ , and  $\lambda = 2.5 \times 10^{-3}$ , and variable  $x_s$ . Note that  $x_s$  shifts proportionally to  $x_c$ , as given in Eq. (13). (Here  $+\eta_1$  denotes a bump configuration and  $-\eta_1$  a gap deformation.)

$\lambda$	$x_s$	$\min(u)$ at $x_c = 9$		$\min(u)$ at $x_c = 8$			$\min(u)$ at $x_c = 7$		
		$+\eta_1$	$-\eta_1$	$x_s$	$+\eta_1$	$-\eta_1$	$x_s$	$+\eta_1$	$-\eta_1$
0		-0.0122	-0.0090		-0.013	-0.0097		-0.0149	-0.0106
$1.25 \times 10^{-3}$	7.5	-0.0092	-0.0067	6.5	-0.0104	-0.0072	5.5	-0.0117	-0.0077
$2.5 \times 10^{-3}$	7.5	0	0	6.5	-0.0011	0	5.5	-0.0017	-0.0001
$1.25 \times 10^{-3}$	8	-0.0091	-0.0066	7	-0.0103	-0.0071	6	-0.0117	-0.0077
$2.5 \times 10^{-3}$	8	0	0	7	-0.0009	0	6	-0.0017	0
$1.25 \times 10^{-3}$	8.5	-0.0088	-0.0067	7.5	-0.0099	-0.0072	6.5	-0.0113	-0.0078
$2.5 \times 10^{-3}$	8.5	0	-0.0004	7.5	0	-0.0004	6.5	-0.0010	-0.0005

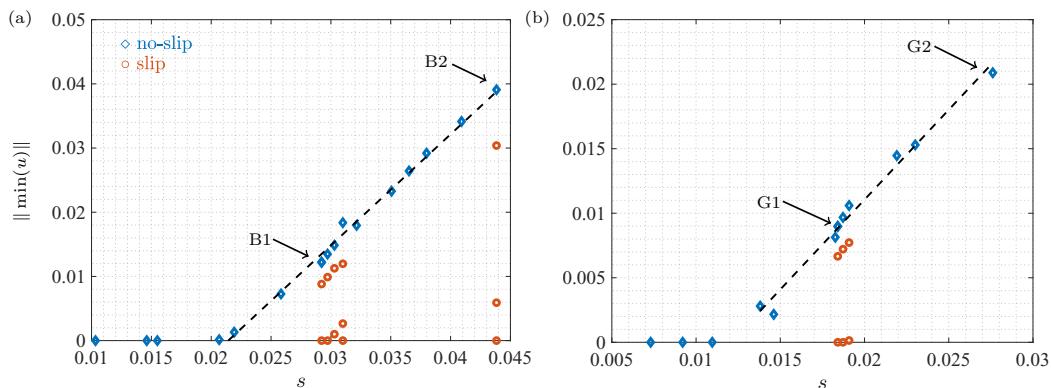


FIG. 6. Absolute value of the minimum of the streamwise  $u$  velocity,  $\|\min(u)\|$ , found within the region of separation, as a function of  $s = h/(x_c^\alpha \sigma^\beta)$ , where  $\alpha = 0.14$ . (a) Bumps with  $\beta = 0.5$  and (b) gaps with  $\beta = 0.33$ . No-slip surfaces are represented by blue diamonds, while slip surfaces with slip lengths  $\lambda \in [1.25 \times 10^{-3}, 7.5 \times 10^{-3}]$  are marked by red circles. Labels B1, B2, G1, and G2 denote those no-slip cases discussed in Sec. IV.

## IV. EFFECT OF SLIP ON SINGLE-SURFACE DEFORMATIONS

### A. Flow separation established by surface deformations

DNS of bump and gap deformations, characterized by aspect ratios given in Table I, are modeled to ascertain the intensity of the separation bubble that emerges along the rear side of the bump and within the gap concavity. In addition, the streamwise center of the bump and gap deformations is varied, with  $x_c \in [7, 9]$ . Once solutions attain a steady state (realized by time  $t = 20$ ), the minimum value of the streamwise  $u$  velocity,  $\min(u)$ , is computed. Figure 6 depicts the size of  $\|\min(u)\|$  found within the separation bubble as a function of

$$s = \frac{h}{x_c^\alpha \sigma^\beta}, \quad (14)$$

where  $\alpha = 0.14$  for both bump and gap configurations, while  $\beta = 0.5$  for bumps and  $\beta = 0.33$  for gaps. Equation (14) was extracted empirically, following a similar procedure to that adopted by Wie and Malik [52] and Thomas *et al.* [53] to correlate features characterizing the surface deformations (i.e., height  $h$ , width  $\sigma$ , and center  $x_c$ ) with the magnitude of the separation bubble. Blue diamond and red circle markers represent those solutions matched to no-slip conditions on the wall and slippery walls with slip lengths  $\lambda \in [1.25 \times 10^{-3}, 7.5 \times 10^{-3}]$ , respectively. In the case of no slip, for bumps that establish regions of separated flow [i.e.,  $\min(u) < 0$ ,

$$\|\min(u)\| \approx 1.7s + p, \quad (15)$$

where  $p \approx -0.04$ . On the other hand, for gaps

$$\|\min(u)\| \approx 1.4s + q, \quad (16)$$

where  $q \approx -0.02$ . Empirical relationships (15) and (16) are depicted by dashed lines in Figs. 6(a) and 6(b), passing through the data points obtained for the surface deformations subject to no-slip conditions. Furthermore, for no-slip boundary conditions, bumps and gaps establish regions of separated flow if

$$s \gtrsim 0.02 \quad \text{and} \quad s \gtrsim 0.012, \quad (17a,b)$$

respectively. For slip surfaces with a relatively small slip length,  $\lambda = 1.25 \times 10^{-3}$ , the magnitude of the minimum velocity,  $\|\min(u)\|$ , exhibits similar trends to those displayed for the no-slip scenario.

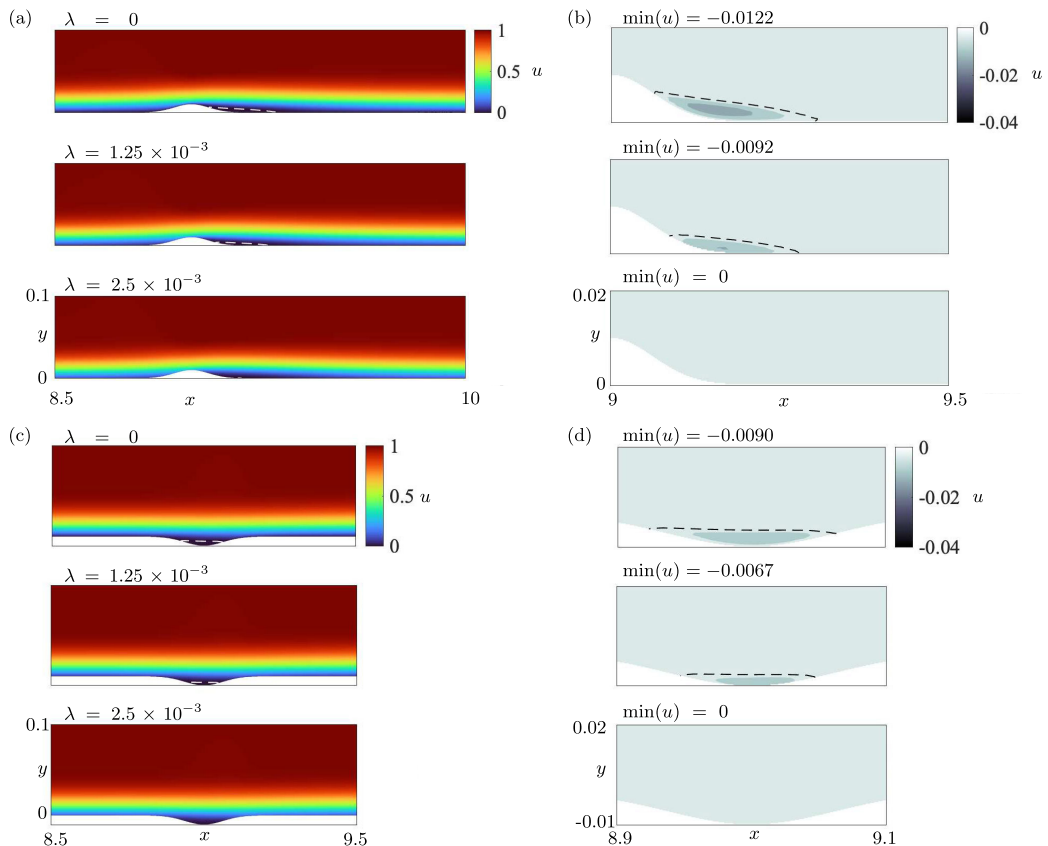


FIG. 7. Contour plots of the streamwise  $u$  velocity, at time  $t = 20$ , for surface deformations with aspect ratio  $\eta_1$  for (a) bump and (c) gap deformations. Secondary plots (b) and (d) highlight the corresponding regions of flow separation, i.e.,  $u < 0$ . The slip length  $\lambda = 0$ ,  $\lambda = 1.25 \times 10^{-3}$ , and  $\lambda = 2.5 \times 10^{-3}$ , and the minimum value of the streamwise  $u$  velocity,  $\min(u)$ , is specified in each case.

The red circles immediately below the dashed lines increase at a rate comparable with that specified in Eqs. (15) and (16), but with reduced  $y$  intercepts  $p$  and  $q$ . However, as the slip length  $\lambda$  increases and the region of separated flow diminishes, causing  $\|\min(u)\|$  to approach zero, the relationship between  $\|\min(u)\|$  and  $s$  becomes increasingly uncertain.

The effect of a slippery surface on the flow over a single isolated surface deformation is described below for those cases labeled B1, B2, G1, and G2 in Fig. 6, corresponding to aspect ratios  $\eta_1 = 0.16$  (B1 and G1, small deformations) and  $\eta_2 = 0.24$  (B2 and G2, large deformations), respectively.

### B. Aspect ratio $\eta_1$ , i.e., small surface deformations

Results are first presented for small surface deformations with aspect ratio  $\eta_1$ , labeled B1 and G1, in Fig. 6. In this case, the  $\bar{x}$  range of the computational domain is given as  $\Omega_{\bar{x}} = [5, 10]$ , i.e.,  $x_{\max} = 10$ .

Figures 7(a) and 7(c) display contour plots of the streamwise  $u$  velocity that develops over the small bump and gap deformations, in the instance the slip length  $\lambda = 0$ ,  $\lambda = 1.25 \times 10^{-3}$ , and  $\lambda = 2.5 \times 10^{-3}$ . Like Fig. 3, the color scheme sets the minimum and maximum of the streamwise  $u$  velocity to zero (dark blue) and unity (dark red), respectively. Therefore, reversed flow, where  $u < 0$ , is matched to dark blue contours. Secondary plots on the right-hand side of Fig. 7 [see Figs. 7(b)

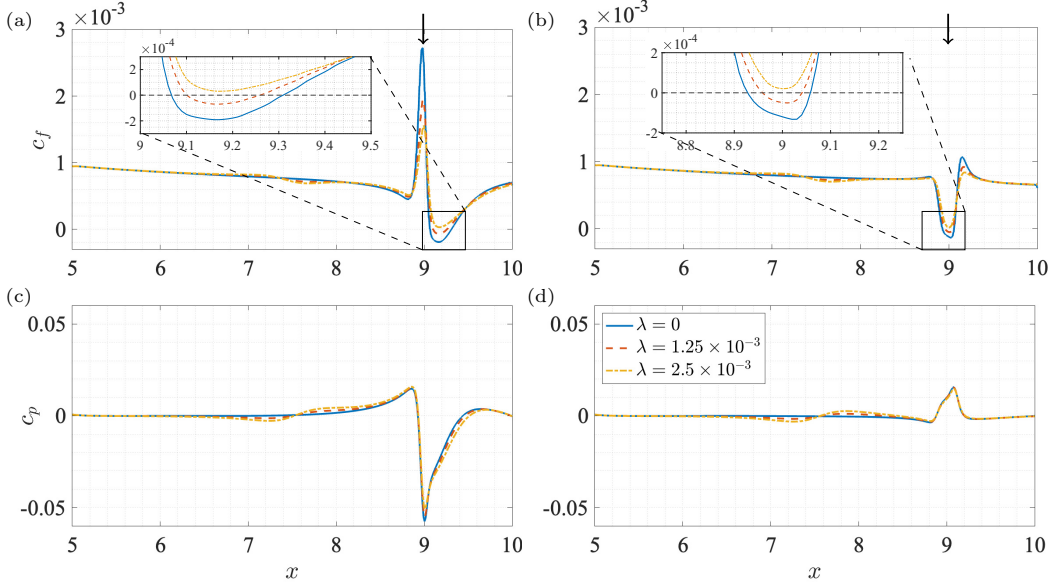


FIG. 8. Distributions of the (a), (b) skin-friction coefficient  $c_f$  and (c), (d) pressure coefficient  $c_p$  for surface deformations with aspect ratio  $\eta_1$ . (a), (c) Bump and (b), (d) gap deformations, for slip lengths  $\lambda = 0$  (solid blue lines),  $\lambda = 1.25 \times 10^{-3}$  (dashed red), and  $\lambda = 2.5 \times 10^{-3}$  (chain yellow). Arrows in (a) and (b) indicate the location of the bump and gap, respectively.

and 7(d)] magnify the regions of separated flow along the rear side of the bump and within the gap concavity, focusing on  $u < 0$ . As the slip length  $\lambda$  increases, the dimensions of the separation bubble along the rear side of the bump shrink. Similarly, the separation pocket within the gap concavity becomes thinner as  $\lambda$  increases. Ultimately, flow separation is inhibited in both cases for the slip length  $\lambda = 2.5 \times 10^{-3}$ .

Skin-friction and pressure distributions on the flat plate are given by the nondimensional coefficients [54]

$$c_f(x) = \frac{2\tau_w^*(x)}{\rho^*U_\infty^{*2}} \quad \text{and} \quad c_p(x) = \frac{2p^*(x)}{\rho^*U_\infty^{*2}}, \quad (18a,b)$$

where  $\tau_w^* = \tau_w^*(x)$  denotes the shear stress at the wall, given by

$$\tau_w^* = \mu^* \left. \frac{\partial u^*}{\partial y^*} \right|_w, \quad (19)$$

where  $\mu^*$  is the dynamic viscosity of the fluid and  $w$  references the wall. Figure 8 illustrates the skin-friction coefficient  $c_f$  and pressure coefficient  $c_p$  distributions for those surface deformations and slip lengths  $\lambda$ , modeled in Fig. 7. About  $x \approx 7.5$ ,  $c_f$  and  $c_p$  exhibit waviness due to the transition from no-slip to slip boundary conditions. For the bump deformation [see Fig. 8(a)],  $c_f$  increases along the front side before decreasing sharply along the rear side. In contrast,  $c_f$  decreases along the left side of the gap and increases along the right side [see Fig. 8(b)]. Both deformations display negative-valued  $c_f$  when  $\lambda = 0$ , with separation pockets forming in the gap concavity and along the rear side of the bump at  $x_{se} \approx 9.07$  and reattaching at  $x_{re} \approx 9.3$ . Surface slip increases  $c_f$  for both configurations;  $\lambda = 2.5 \times 10^{-3}$  establishes  $c_f > 0$  for all streamwise  $x$  positions, ensuring the flow remains attached. The pressure distribution  $c_p$  displays similar variations near the bump and gap [see Figs. 8(c) and 8(d)]. However, slip has little influence on the size and behavior of  $c_p$ .

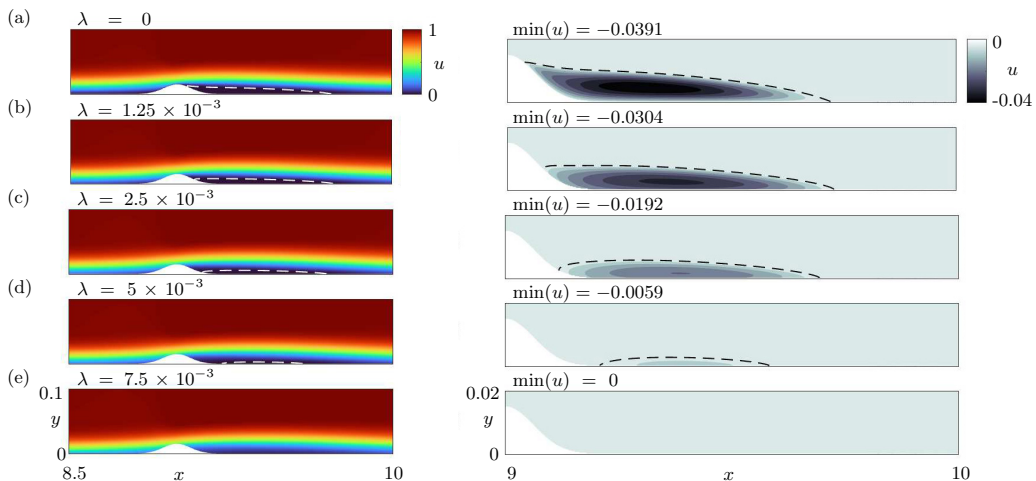


FIG. 9. Contour plots of the streamwise  $u$  velocity, at time  $t = 20$ , for bump deformations centered at  $x_c = 9$  with aspect ratio  $\eta_2$  and slip lengths (a)  $\lambda = 0$ , (b)  $\lambda = 2.5 \times 10^{-3}$ , (c)  $\lambda = 3.75 \times 10^{-3}$ , (d)  $\lambda = 5 \times 10^{-3}$ , and (e)  $\lambda = 7.5 \times 10^{-3}$ . Secondary plots on the right highlight the region of flow separation, where  $u < 0$ . The minimum of the streamwise  $u$  velocity,  $\min(u)$ , is specified for each slip length,  $\lambda$ .

In the case of no slip, curvature on the front side of the bump (or the left side of the gap) induces a deceleration of the fluid and a pressure increase. The pressure change creates an unfavorable pressure gradient, thickens the boundary layer, and slows the flow until separation occurs. Downstream of the separation point, a wake characterized by recirculating flow and low-pressure forms. The location of flow reattachment depends on the shape of the bump and gap deformation. The slip condition enhances the mean flow near the plate surface, increasing the momentum flux, which overcomes the adverse pressure gradient for sufficiently large slip lengths. Thus, a slippery surface allows the flow to reattach sooner and eliminates flow separation.

### C. Aspect ratio $\eta_2$ , i.e, large surface deformations

An equivalent analysis is presented for the large surface deformations with aspect ratio  $\eta_2$ , labeled B2 and G2, in Fig. 6. In this case, the  $\bar{x}$  range of the computational domain  $\Omega_{\bar{x}} = [5, 11]$ , i.e.,  $x_{\max} = 11$ . Due to the larger dimensions of the separation bubble found along the rear side of the bump,  $x_{\max}$  was increased to 11 to avoid the location of flow reattachment being too close to the outflow boundary. Thus, ensuring the flow at the outlet boundary remains unidirectional.

Figure 9 displays contour plots of the streamwise  $u$  velocity that develops over the large bump centered about  $x_c = 9$ , with slip lengths  $\lambda \in [0, 7.5 \times 10^{-3}]$ . Secondary plots on the right-hand side highlight the separation bubble, where  $u < 0$ . Similar to those results presented in Figs. 7(a) and 7(b), a separation bubble forms along the rear side of the bump, but with greater dimensions than those established for the small deformation of aspect ratio  $\eta_1$ , with a larger slip length  $\lambda$ , required to inhibit flow separation.

For a flow that separates and reattaches about the respective streamwise locations  $x_{\text{se}}$  and  $x_{\text{re}}$ , the length of the separation bubble is defined as

$$L_b = x_{\text{re}} - x_{\text{se}}. \quad (20)$$

For  $\lambda = 0$ , the flow separates at  $x_{\text{se}} \approx 9.03$  and reattaches at  $x_{\text{re}} \approx 9.7$ , establishing a pocket of separated flow of streamwise length  $L_b \approx 0.67$ . Here,  $L_b$  is more than double the length of the separation bubble that forms behind the small bump of aspect ratio  $\eta_1$ , where  $L_b \approx 0.3$  [recall Figs. 7(a) and 7(b)]. Surface slip again reduces the dimensions of the separation bubble; the

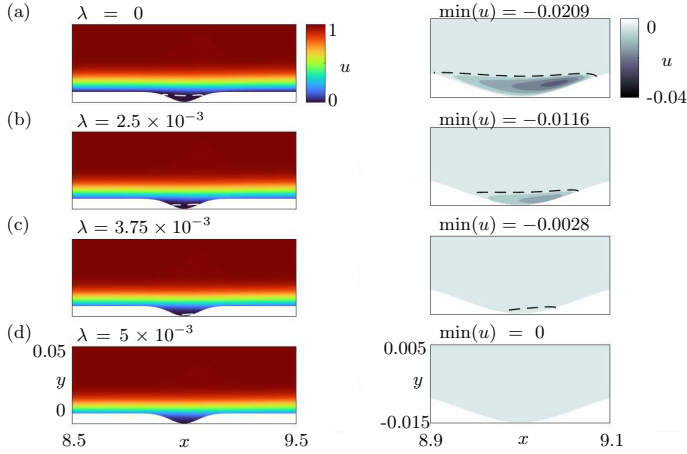


FIG. 10. Same as Fig. 9 but for the gap deformation of aspect ratio  $\eta_2$  and slip lengths (a)  $\lambda = 0$ , (b)  $\lambda = 2.5 \times 10^{-3}$ , (c)  $\lambda = 3.75 \times 10^{-3}$ , and (d)  $\lambda = 5 \times 10^{-3}$ .

thickness shrinks and the flow reattaches sooner. As slip increases,  $x_{se}$  shifts downstream, along the rear side of the bump, while  $x_{re}$  moves upstream. Eventually, for the slip length  $\lambda = 7.5 \times 10^{-3}$ ,  $x_{se}$  and  $x_{re}$  coalesce, and the flow no longer separates.

Figure 10 depicts the same behavior as Fig. 9, but for the large gap deformation with aspect ratio  $\eta_2$  and slip lengths  $\lambda \in [0, 5 \times 10^{-3}]$ . For  $\lambda = 5 \times 10^{-3}$ , the minimum streamwise  $u$  velocity,  $\min(u) = 0$ . Thus, a smaller slip length  $\lambda$  inhibits separation within the gap concavity than is needed for the bump configuration.

Profiles of the streamwise  $u$  velocity are plotted in Fig. 11 versus the wall-normal  $y$  direction at  $x = 9.5$  for the bump deformation and at  $x = 9$  for the gap concavity. These streamwise locations coincide with the respective regions of flow separation. The  $u$  velocity in Fig. 11(a) is negative near the wall for all slip lengths  $\lambda \leq 5 \times 10^{-3}$ , indicating reversed flow. (However,  $u = 0$  at  $y = 0$  when  $\lambda = 0$  due to the no-slip boundary condition.) The  $u$  velocity near the wall increases as the slip length  $\lambda$  increases. Eventually, for  $\lambda = 7.5 \times 10^{-3}$ ,  $u > 0$  for all wall-normal  $y$  locations, i.e.,

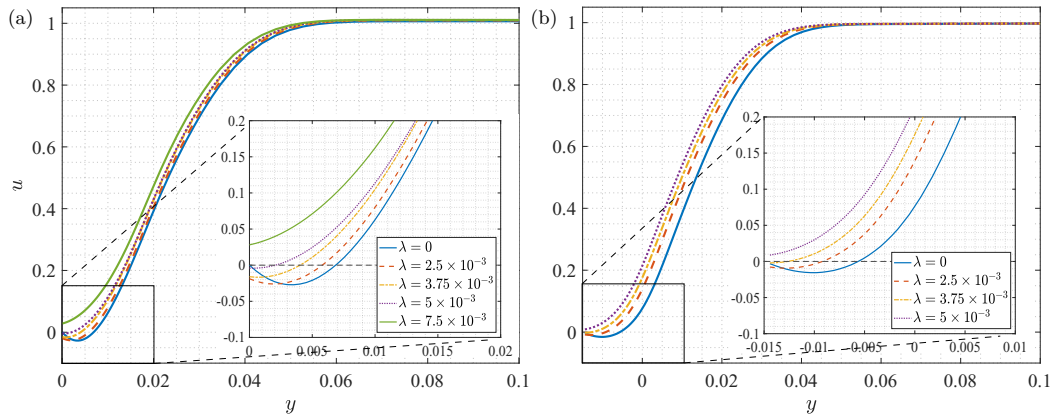


FIG. 11. Velocity profiles at (a)  $x = 9.5$  for the bump and (b)  $x = 9$  for the gap deformations. The aspect ratio is  $\eta_2$  and slip lengths  $\lambda = 0$  (solid blue lines),  $\lambda = 2.5 \times 10^{-3}$  (dashed red),  $\lambda = 3.75 \times 10^{-3}$  (chain yellow),  $\lambda = 5 \times 10^{-3}$  (dotted purple), and  $\lambda = 7.5 \times 10^{-3}$  (solid green).

TABLE III. Streamwise locations for separation  $x_{se}$  and reattachment  $x_{re}$  for the small (B1) and large (B2) bump configurations centered at  $x = 9$ , and thickness  $T$  of the reversed flow region that forms within the small (G1) and large (G2) gap deformations located at  $x = 9$ .

$\lambda$	B1 ( $\eta_1$ )		G1 $T$	B2 ( $\eta_2$ )		G2 $T$
	$x_{se}$	$x_{re}$		$x_{se}$	$x_{re}$	
0	9.065	9.315	0.0065	9.040	9.710	0.0115
$1.25 \times 10^{-3}$	9.100	9.260	0.0040			
$2.5 \times 10^{-3}$	No separation		No separation	9.075	9.700	0.0075
$3.75 \times 10^{-3}$				9.125	9.660	0.0025
$5 \times 10^{-3}$				9.235	9.525	No separation
$7.5 \times 10^{-3}$				No separation		

no separation occurs. Similarly, in Fig. 11(b),  $u < 0$  near the plate surface for all  $\lambda \leq 3.75 \times 10^{-3}$ , and  $u > 0$  is realized for  $\lambda = 5 \times 10^{-3}$ . Moreover, for the bump configuration, the flow recovers the free-stream velocity  $u = 1$  near  $y \approx 0.06$ , whereas for the gap deformation,  $u = 1$  about  $y \approx 0.04$ .

An estimate for the wall-normal  $y$  interval  $T$  that the flow reverses direction is computed using the plots of the  $u$  velocity in Fig. 11. The thickness

$$T = y_1 - y_0, \quad \text{such that} \quad \begin{cases} u < 0, & y_0 < y < y_1 \\ u > 0, & \text{otherwise} \end{cases} \quad (21)$$

giving  $T \approx 7 \times 10^{-3}$  and  $T \approx 5 \times 10^{-3}$  for the respective bump and gap deformations, in the instance  $\lambda = 0$ , i.e., no slip. Results demonstrate that as the slip length  $\lambda$  increases,  $T$  decreases. The region of reversed flow along the rear side of the bump (or within the gap) becomes thinner. In particular, the thickness  $T$  is reduced by half for  $\lambda = 3.75 \times 10^{-3}$  and  $\lambda = 2.5 \times 10^{-3}$  for the respective bump and gap configurations.

Table III presents the separation and reattachment locations  $x_{se}$  and  $x_{re}$  for the small and large bumps, along with the thickness  $T$  of the reversed flow region that forms within the small and large gaps. The length of the separation bubble  $L_b$  that forms downstream of the two bumps located at  $x = 9$  of aspect ratio  $\eta_1$  (blue circle markers) and  $\eta_2$  (red squares) are plotted in Fig. 12(a) as functions of the slip length  $\lambda$ . Figure 12(b) presents an equivalent plot of the thickness  $T$  of the

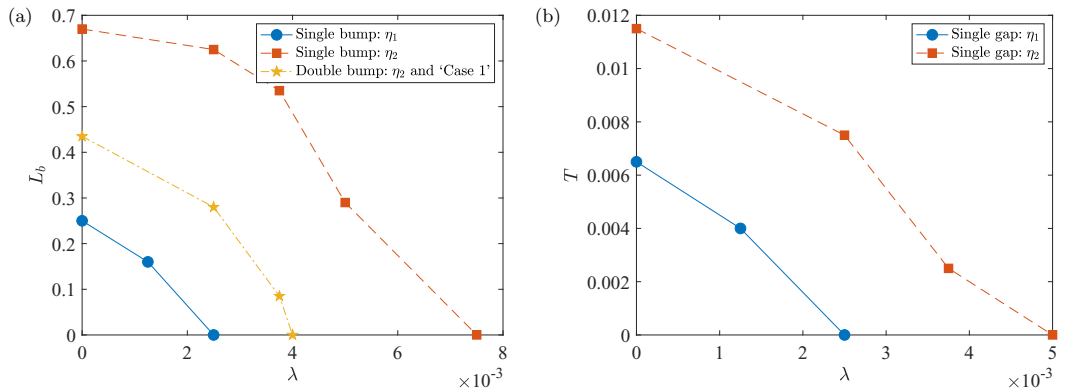


FIG. 12. (a) Streamwise length of the separation bubble  $L_b$  that forms downstream of the bump located at  $x = 9$  for the single-bump configurations  $\eta_1$  (blue circle markers) and  $\eta_2$  (red squares), and the double-bump configuration “case 1” (yellow stars). (b) Thickness  $T$  of the reversed flow region that forms in the gap concavities located at  $x = 9$  for  $\eta_1$  (blue circles) and  $\eta_2$  (red squares).



reversed flow region that forms in the two gap concavities at  $x = 9$  for  $\eta_1$  (blue circles) and  $\eta_2$  (red squares). The two illustrations demonstrate the significant control of flow separation as  $\lambda$  increases.

As expected, larger slip lengths  $\lambda$  are necessary to counteract flow separation established by bump and gap deformations with aspect ratio  $\eta_2$ , compared to the smaller deformations with aspect ratio  $\eta_1$ . For the bump configuration, slip lengths  $\lambda = 2.5 \times 10^{-3}$  and  $\lambda = 7.5 \times 10^{-3}$  prevent flow separation for small and large bumps, respectively. In contrast, for the gap deformations, slip lengths  $\lambda = 2.5 \times 10^{-3}$  and  $\lambda = 5 \times 10^{-3}$  are enough to suppress flow separation for small and large gaps. Notably, for deformations of the same aspect ratio, gaps produce a weaker recirculation region than bumps and, thus, require a smaller slip length to inhibit flow separation. Hence, the flow dynamics for a single-bump setup align with the numerical results found in [55]. In that study, a superhydrophobic surface was shown to counteract flow separation in turbulent channel flow and reduce form drag.

## V. EFFECT OF SLIP ON DOUBLE-BUMP CONFIGURATIONS

In the previous section, we demonstrated that bumps create larger-sized pockets of separated flow than gaps. Nevertheless, a sufficiently large slip length  $\lambda$  can control flow separation induced by a single-bump deformation. Building upon the work of single-bump deformations, Marquillie and Ehrenstein [1] considered the flow over a double-bump geometry with no-slip boundary conditions applied to the flat plate. They modeled a second bump downstream of the first to act as a stabilizing mechanism. For bumps far enough apart, the separation bubble that formed between the two bumps was characterized by oscillatory behavior and low-frequency flapping. However, decreasing the gap between the two bump deformations eliminated this phenomenon. In addition, the regions of flow separation were reduced.

Here, we extend our analysis from a single-bump to a double-bump configuration with slip applied to the plate surface to control flow separation. Two distinct double-bump configurations are modeled, with each bump having an aspect ratio  $\eta_2$ , i.e., large bumps. In the first configuration, “case 1,” the two bumps are located at  $x_c = 8.5$  and 9, and in the second setting, “case 2,” bumps are located further apart, with the first bump shifted upstream to  $x_c = 8$ .

### A. Case 1

In the first double-bump configuration, bumps are located close to each other at the streamwise positions  $x_c = 8.5$  and 9. The  $\bar{x}$  range of the computational domain  $\Omega_{\bar{x}} = [5, 11]$ , i.e.,  $x_{\max} = 11$ .

Figure 13 displays contour plots of the streamwise  $u$  velocity for slip lengths  $\lambda \in [0, 6 \times 10^{-3}]$ , revealing two pockets of separated flow. One separation pocket forms in the gap between the two bumps and a second along the rear side of the second bump, consistent with the behavior of Marquillie and Ehrenstein [1]. Similar to the separation bubble within the gap concavities depicted in Figs. 7(c) and 7(d) and 10, the intensity of the separated flow between the two bumps peaks near the front side of the second bump. In the no-slip case [see Fig. 13(a)], the separation bubble downstream of the second bump is shorter compared to the single-bump configuration [see Fig. 9(a)]. In fact, for the double-bump arrangement, the flow separates at  $x_{se} \approx 9.05$  and reattaches at  $x_{re} \approx 9.45$ , whereas  $x_{re} \approx 9.70$  for the single-bump model. Hence, the length of this separation bubble for the double- and single-bump configurations is  $L_b \approx 0.40$  and  $L_b \approx 0.65$ , respectively. Thus, the first bump controls the size of the separation bubble downstream of the second bump, similar to [1]. Moreover, the separation bubble along the rear side of the second bump is inhibited for a slip length  $\lambda = 4 \times 10^{-3}$  for the double-bump configuration [see Fig. 13(d)], compared with  $\lambda = 7.5 \times 10^{-3}$  for the single-bump configuration [see Fig. 9(e)]. [This particular observation is illustrated in Fig. 12(a), with yellow stars representing the solutions for the double-bump arrangement.] In addition, the recirculation region between the two bumps is suppressed by a slip length  $\lambda = 6 \times 10^{-3}$  [see Fig. 13(f)]. Thus, the double-bump arrangement requires a reduced level of slip to eliminate all pockets of separated flow.

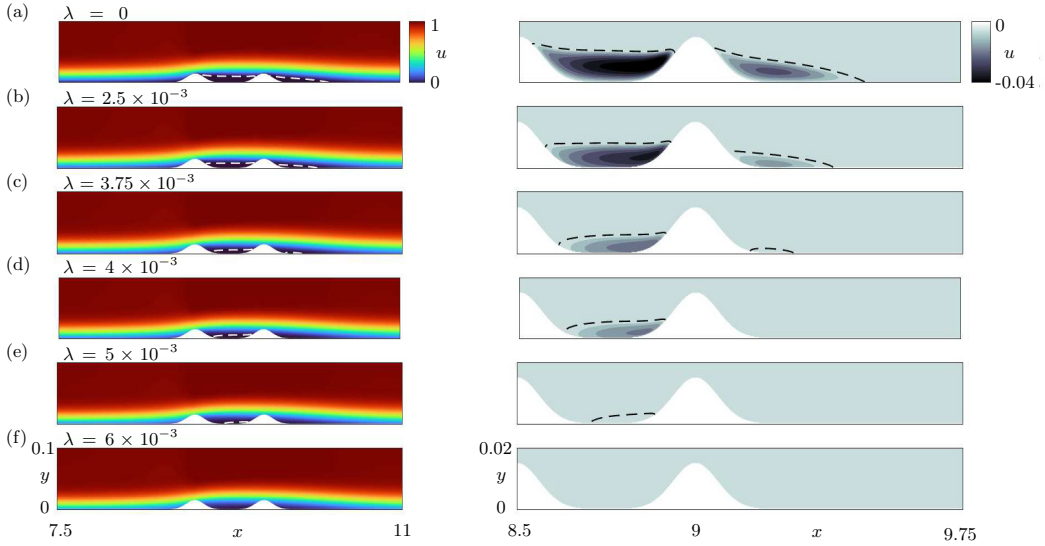


FIG. 13. Contour plots of the streamwise  $u$  velocity, at time  $t = 20$ , for the double-bump configuration “case 1” and slip lengths (a)  $\lambda = 0$ , (b)  $\lambda = 2.5 \times 10^{-3}$ , (c)  $\lambda = 3.75 \times 10^{-3}$ , (d)  $\lambda = 4 \times 10^{-3}$ , (e)  $\lambda = 5 \times 10^{-3}$ , and (f)  $\lambda = 6 \times 10^{-3}$ . Secondary plots on the right highlight the region of flow separation, where  $u < 0$ .

Distributions of the skin-friction coefficient  $c_f$  and pressure coefficient  $c_p$  are illustrated in Fig. 14. In the case of no slip, the  $c_f$  curve displays two distinct peaks at the streamwise locations  $x = 8.5$  and  $9$ , which align with the tips of the two bumps. At  $x = 9$ , the peak reaches  $c_f \approx 2.2 \times 10^{-3}$ , which is notably lower than the  $c_f \approx 3.7 \times 10^{-3}$  observed at  $x = 8.5$ . When compared to the single-bump model in Fig. 8(a) where  $c_f \approx 2.7 \times 10^{-3}$  at  $x = 9$ , it is evident that the  $c_f$  values at  $x = 8.5$  and  $9$  are higher and lower, respectively. Furthermore, the two local minima in  $c_f$  are of similar size to that realized for the single-bump geometry. With an increase in the slip length  $\lambda$ , the magnitude of  $c_f$  about the two peaks diminishes, while it augments about the

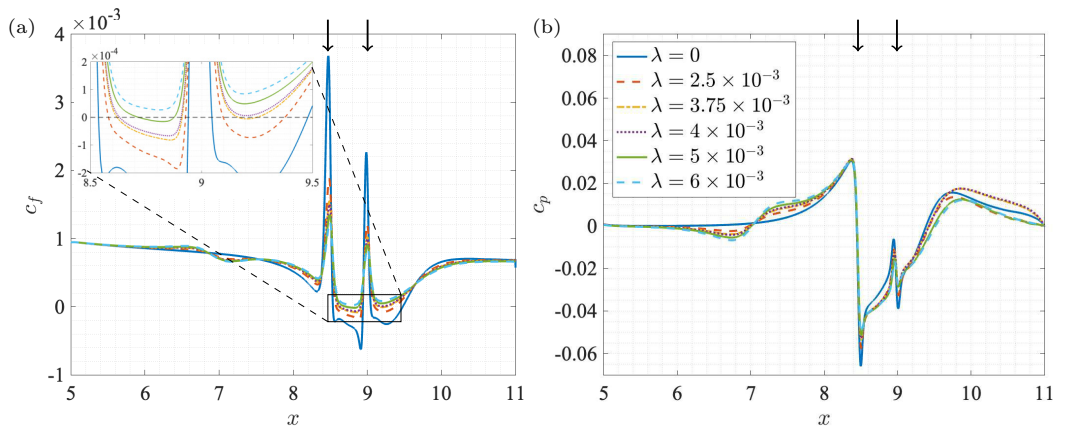


FIG. 14. Distributions of the (a) skin-friction coefficient  $c_f$  and (b) pressure coefficient  $c_p$  for the double-bump configuration case 1, for slip lengths  $\lambda = 0$  (solid blue lines),  $\lambda = 2.5 \times 10^{-3}$  (dashed red),  $\lambda = 3.75 \times 10^{-3}$  (chain yellow),  $\lambda = 4 \times 10^{-3}$  (dotted purple),  $\lambda = 5 \times 10^{-3}$  (solid green), and  $\lambda = 6 \times 10^{-3}$  (dashed light blue). Arrows in (a) and (b) indicate the locations of the two bumps.

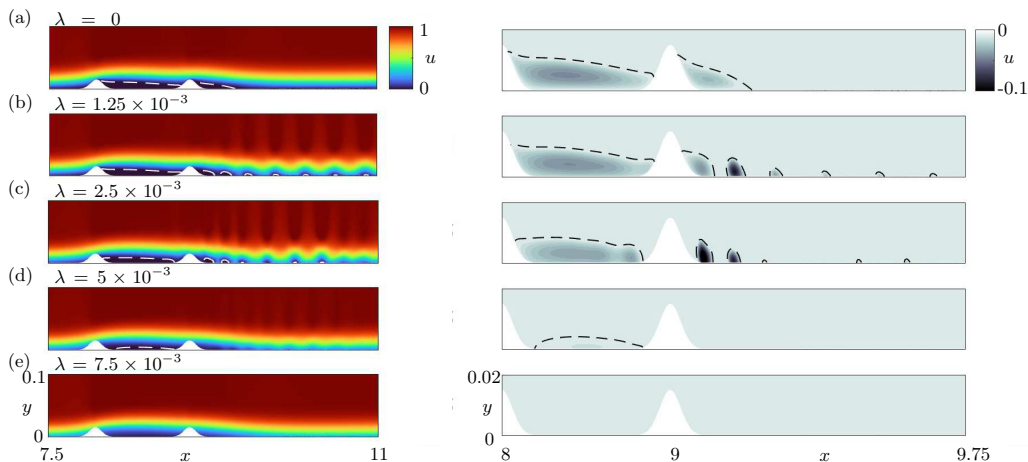


FIG. 15. Same as Fig. 13 but for the double-bump configuration case 2, and slip lengths (a)  $\lambda = 0$ , (b)  $\lambda = 1.25 \times 10^{-3}$ , (c)  $\lambda = 2.5 \times 10^{-3}$ , (d)  $\lambda = 5 \times 10^{-3}$ , and (e)  $\lambda = 7.5 \times 10^{-3}$ . Secondary plots on the right highlight the region of flow separation, where  $u < 0$ .

two troughs. Specifically, for a slip length  $\lambda = 4 \times 10^{-3}$ , a positive  $c_f$  is realized on the streamwise interval  $9 < x < 9.5$ . Meanwhile, when  $\lambda = 6 \times 10^{-3}$ ,  $c_f > 0$  in the range  $8.5 < x < 9$ , which is consistent with the behavior shown in Fig. 13.

The pressure coefficient  $c_p$  displays two local minima. The first corresponds to the bump at  $x = 8.5$  where  $c_p \approx -0.065$  for the no-slip case, and the second minimum corresponds to the second bump at  $x = 9$ , where  $c_p \approx -0.04$ . This is similar to the pressure coefficient  $c_p \approx -0.055$  obtained for the single-bump model in Fig. 8(b). In both instances, slip slightly reduces the intensity of the pressure coefficient  $c_p$  at the peaks of the bumps. For no-slip and moderate slip lengths (including  $\lambda = 2.5 \times 10^{-3}$  and  $\lambda = 3.75 \times 10^{-3}$ ),  $c_p$  decreases sharply near the outlet boundary. However, this does not have a measurable upstream influence on the behavior near the bumps.

## B. Case 2

In the second double-bump configuration, bumps are located further apart and centered at the streamwise positions  $x_c = 8$  and  $9$ . In this instance, the computational domain along the  $\bar{x}$  direction is  $\Omega_{\bar{x}} = [5, 12]$ , i.e.,  $x_{\max} = 12$ . A larger computational domain is necessary as new dynamic features emerge. In addition, the streamwise location  $x_s$ , at which the wall condition transitions from no slip to slip, is shifted upstream to  $x_s = 7$ .

Contour plots of the streamwise  $u$  velocity are displayed in Fig. 15 of the flow that develops over this double-bump configuration, with slip lengths  $\lambda \in [0, 7.5 \times 10^{-3}]$ . In the no-slip case, two pockets of separated flow emerge, similar to the behavior observed in case 1 [see Fig. 13(a)]. First, an extended pocket of flow separation forms in the gap between the two bumps. However, unlike case 1, where the intensity of the separated flow peaks along the front side of the second bump, a peak intensity is attained near the gap center at  $x = 8.5$ . In addition, a second region of separation develops along the rear side of the second bump. The flow separates about the second bump at  $x_{\text{se}} \approx 9.05$  and reattaches at  $x_{\text{re}} \approx 9.5$ , forming a separation bubble of length  $L_b \approx 0.45$ . Hence, the separation bubble is again shorter than the  $L_b \approx 0.65$  observed for the single-bump arrangement [see Fig. 9(a)]. Nonetheless, the length of the separation pocket exceeds that depicted in case 1, where  $L_b \approx 0.4$ . Thus, the proximity of the two bumps plays a significant role in reducing the dimensions of the separation bubble. Specifically, the size of the separated flow along the rear side of the second bump decreases as the bumps move closer together.

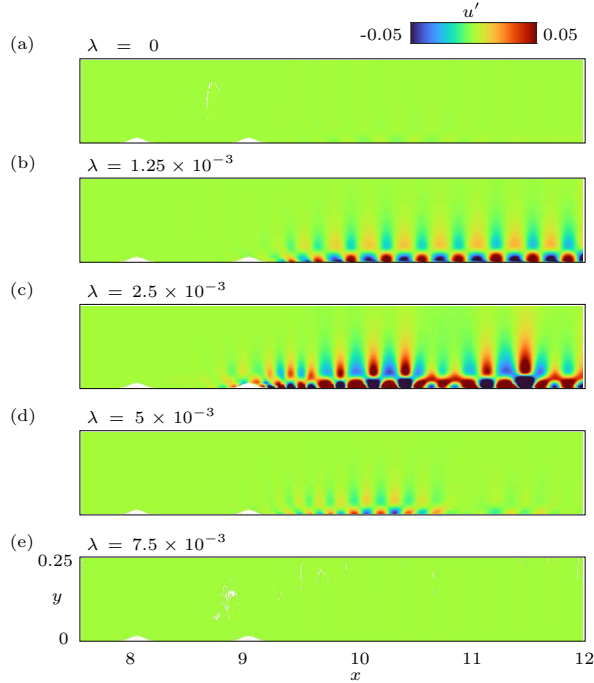


FIG. 16. Contours of the perturbation  $u'$  (i.e.,  $u' = u - \bar{u}$ ), where  $\bar{u}$  denotes the mean flow, averaged over  $10 < t < 20$ , for the slip lengths (a)  $\lambda = 0$ , (b)  $\lambda = 1.25 \times 10^{-3}$ , (c)  $\lambda = 2.5 \times 10^{-3}$ , (d)  $\lambda = 5 \times 10^{-3}$ , and (e)  $\lambda = 7.5 \times 10^{-3}$ .

The flow dynamics begin to differ when slip is applied to the plate surface. Specifically, for moderate slip lengths,  $\lambda = 1.25 \times 10^{-3}$  and  $\lambda = 2.5 \times 10^{-3}$  [see Figs. 15(b) and 15(c)], the separation bubble in the gap between the two bumps is characterized by two regions of recirculating flow, where the second, smaller pocket of separated flow detaches from the primary separation bubble, at a streamwise location upstream of the second bump. Along the rear side of the second bump, the flow exhibits nonlinear oscillations, resulting in unsteady pockets of separated flow that propagate downstream before dissipating. (A more detailed discussion of this phenomenon is given below.) However, a noticeable shift occurs when the slip length  $\lambda$  is increased to  $\lambda = 5 \times 10^{-3}$ . In this instance, the flow does not separate behind the second bump [see Fig. 15(d)]. In addition, the oscillatory behavior has disappeared, with flow separation confined to the interval between the two bump deformations. Moreover, further increases in the slip length suppress this separation bubble, with  $\lambda = 7.5 \times 10^{-3}$  eliminating all pockets of separated flow, as shown in Fig. 15(e).

Contour plots of the perturbation  $u' = u - \bar{u}$  are displayed in Fig. 16 at time  $t = 20$  for the same set of slip lengths  $\lambda$ . Here,  $\bar{u}$  represents the mean flow averaged over the time interval  $10 < t < 20$ . For the no-slip case, shown in Fig. 16(a), a small amplitude perturbation emerges that is approximately three orders of magnitude smaller than the  $u$  velocity. This perturbation dissipates as it propagates downstream. In contrast, when there is a relatively small slip length  $\lambda$ , the perturbation  $u'$  exhibits a spatially periodic pattern. For instance, the solution in Fig. 16(b) displays this phenomenon for  $\lambda = 1.25 \times 10^{-3}$ , which is similar in appearance to the observations of Marquillie and Ehrenstein [1] (see Fig. 14 of their paper). As the slip length  $\lambda$  increases, the perturbation  $u'$  is characterized by nonlinear features, as is evident in Fig. 16(c) for  $\lambda = 2.5 \times 10^{-3}$ . Nevertheless, these oscillatory periodic structures diminish for further increases in  $\lambda$ , with  $\lambda = 7.5 \times 10^{-3}$  effectively eliminating these features and all regions of flow separation [see Fig. 16(e)]. Thus, the combination of distance between the two bumps and the slip length  $\lambda$ , given

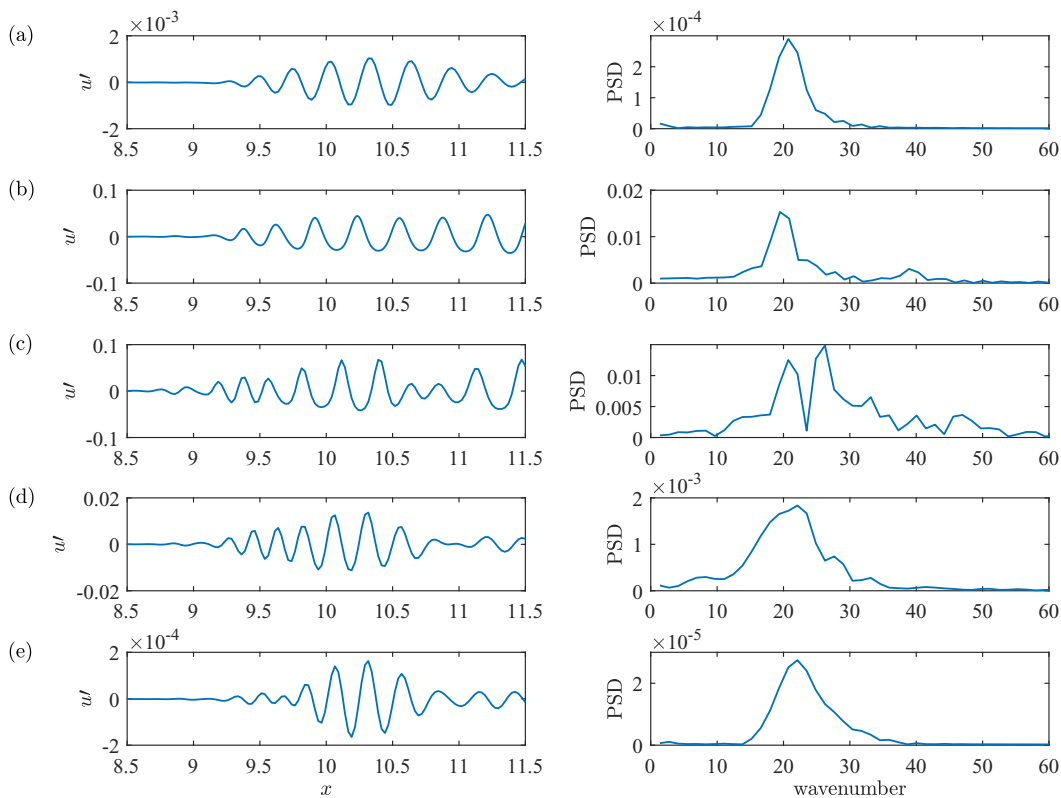


FIG. 17. Spatial evolution of the perturbation  $u'$  (i.e.,  $u' = u - \bar{u}$ ) versus  $x$  at  $y = 0.05$ , where  $\bar{u}$  denotes the mean flow averaged over  $10 < t < 20$ . The slip length (a)  $\lambda = 0$ , (b)  $\lambda = 1.25 \times 10^{-3}$ , (c)  $\lambda = 2.5 \times 10^{-3}$ , (d)  $\lambda = 5 \times 10^{-3}$ , and (e)  $\lambda = 7.5 \times 10^{-3}$ . The corresponding power spectral densities (PSD) are plotted on the right-hand side.

here for case 2, is sufficient to generate periodic structures matching the low-frequency flapping observed by Marquillie and Ehrenstein [1] and others for no-slip surfaces.

Figure 17 displays the perturbation  $u'$  over the streamwise range  $8.5 < x < 11.5$ , at the wall-normal height  $y = 0.05$ , for each slip length  $\lambda$ , modeled in Figs. 15 and 16. In addition, on the right-hand side of Fig. 17, the corresponding power spectral densities (PSD) of the perturbation are plotted versus the wave number. For the no-slip case in Fig. 17(a), the perturbation  $u'$  is of the order  $10^{-3}$ , whereas the PSD exhibits a peak amplitude at a wave number of approximately 20, which aligns with the observed wavelength in the perturbation. For the slip length  $\lambda = 1.25 \times 10^{-3}$ , shown in Fig. 17(b), harmonic behavior emerges, with a secondary smaller peak in the PSD observed at a wave number of approximately 40. Moreover, the amplitude of the perturbation  $u'$  has increased by two orders of magnitude, with  $u' \sim O(10^{-1})$ . A similar sized perturbation  $u'$  is obtained for  $\lambda = 2.5 \times 10^{-3}$  [see Fig. 17(c)]. However, in this instance, the perturbation and the associated PSD exhibit significant nonlinear features. The appearance of two peaks near the wave number 20 likely arises from the limited  $x$  range used in the PSD analysis, and expanding the  $x$  domain may lead to the collapse of these two wave numbers onto a singular wave number. For larger slip lengths  $\lambda = 5 \times 10^{-3}$  and  $\lambda = 7.5 \times 10^{-3}$ , the amplitude of the perturbation  $u'$  diminishes by one and three orders of magnitude, respectively, with  $u'$  once again characterized by linear behavior. Furthermore, the PSD plots indicate that the dominant wave number again corresponds to a value near 20.

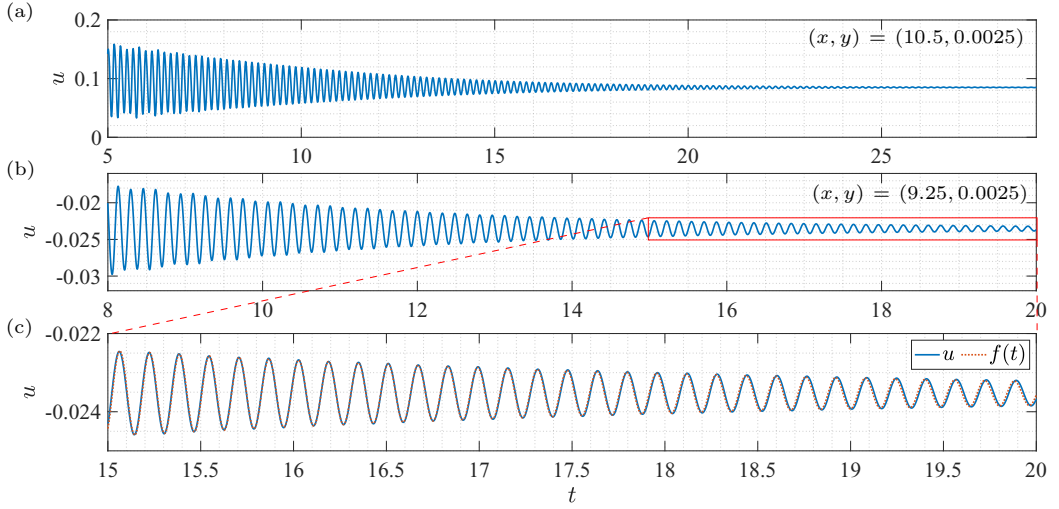


FIG. 18. Time evolution of the streamwise  $u$  velocity for the double-bump configuration case 2 and  $\lambda = 0$ , at (a)  $(x, y) = (10.5, 0.0125)$  and (b)  $(x, y) = (9.25, 0.0125)$ . (c) Same as (b) but over a reduced time range, with a fitting function  $f(t)$  (dotted red), given by Eq. (22).

Further features of the nonlinear oscillatory phenomenon that develops past the two-bump configuration are captured by considering the time development of the flow. The time evolution of the streamwise  $u$  velocity, for  $\lambda = 0$ , is plotted in Fig. 18 at  $(x, y) = (10.5, 0.0125)$ , that is, located downstream of both bump deformations, and  $(x, y) = (9.25, 0.0125)$ , that is, inside the separation bubble along the rear side of the second bump. In each instance, the  $u$  velocity displays decaying oscillatory behavior. After a short transient time interval, oscillations in Fig. 18(a) dissipate, and the solution converges towards a positive constant. Similarly, in Fig. 18(b), oscillations dissipate at large  $t$ . However, a negative-valued  $u$  velocity is attained instead, as this location is inside a separation bubble. The oscillatory behavior of the streamwise  $u$  velocity, in Fig. 18(b), is replotted over a reduced time range in Fig. 18(c). In addition, the exponential decay characterizing the oscillatory behavior of the  $u$  velocity is modeled by the function

$$f(t) = u_0 + A_0 e^{-t/\tau} \sin(2\pi f_0 t + \phi), \quad (22)$$

where  $A_0$  is the amplitude of the oscillations,  $\tau$  is the decay constant,  $f_0$  is the frequency,  $\phi$  is the phase shift, and  $u_0$  is an offset. Setting  $A_0 = 0.0520$ ,  $\tau = 3.8945$ ,  $f_0 = 6.2263$ ,  $\phi = -3.4247$ , and  $u_0 = -0.0235$  establishes the function  $f(t)$  plotted in Fig. 18 (dotted red line) that coincides with the streamwise  $u$  velocity.

Figure 19 displays the time evolution of the streamwise  $u$  velocity at  $(x, y) = (9.5, 0.0125)$  for slip lengths  $\lambda = 1.25 \times 10^{-3}$ ,  $\lambda = 2.5 \times 10^{-3}$ , and  $\lambda = 5 \times 10^{-3}$ , which are associated with nonlinear oscillatory phenomena. Solutions clearly demonstrate the oscillatory behavior of the flow downstream of the second bump. The top three plots [see Figs. 19(a), 19(d), and 19(g)] depict the  $u$  velocity over a longer time interval, while the middle three plots [see Figs. 19(b), 19(e), and 19(h)] illustrate the same solution but over a reduced time interval. There is a marked difference in behavior with that presented above in Fig. 18(c) for the no-slip case. Initially, the amplitude of the oscillating  $u$  velocity increases, and for sufficiently large time  $t$ , nonlinear saturation is achieved, with the flow characterized by periodic behavior; flow dynamics are again similar to that observed by Marquillie and Ehrenstein [1] (see Fig. 12 of their paper).

The power spectral densities (PSD) corresponding to the above time histories are displayed in Figs. 19(c), 19(f), and 19(i). There is clear evidence of a fundamental frequency at  $f \approx 6$  with its harmonics in Fig. 19(c), for the case matched to  $\lambda = 1.25 \times 10^{-3}$ . This behavior is consistent with



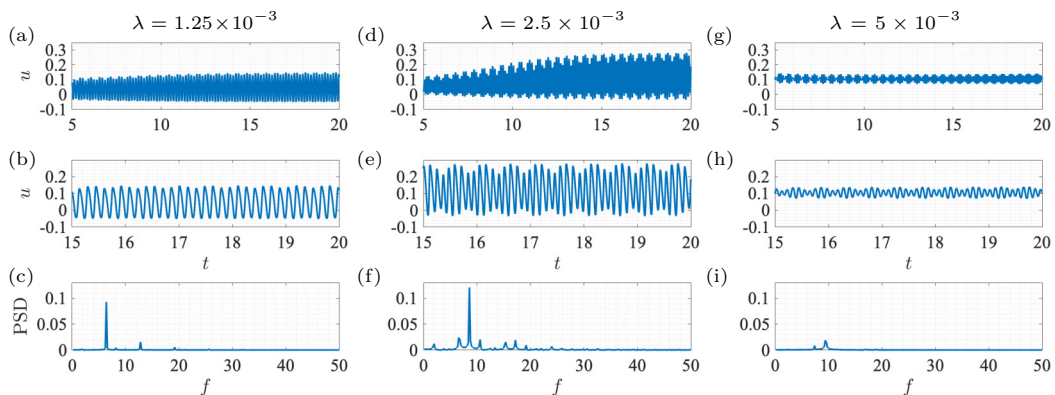


FIG. 19. Time evolution of the streamwise  $u$  velocity for the double-bump configuration case 2, at  $(x, y) = (9.5, 0.0125)$ , for slip lengths (a), (b)  $\lambda = 1.25 \times 10^{-3}$ , (d), (e)  $\lambda = 2.5 \times 10^{-3}$ , and (g), (h)  $\lambda = 5 \times 10^{-3}$ . (c), (f), (i) Display the corresponding power spectral densities (PSD) as a function of the frequency,  $f$ .

the results obtained for the no-slip case, presented in Fig. 18(c), in which there were approximately six oscillations per unit of time. The primary frequency is higher in Fig. 19(f), for  $\lambda = 2.5 \times 10^{-3}$ , with  $f \approx 8$ , whereas  $f \approx 10$  in Fig. 19(i) for  $\lambda = 5 \times 10^{-3}$ , but the signal amplitude has reduced considerably. Thus, oscillatory behavior dissipates for an increasing slip length  $\lambda$ , and disappears for  $\lambda = 7.5 \times 10^{-3}$ , which is greater than that required for case 1 and comparable with that needed for the single-bump arrangement (see Fig. 9).

Several experimental and numerical studies, including [1–3,6,56], have reported the onset of nonlinear oscillations in separated flows with no-slip walls and refer to this phenomenon as low-frequency flapping. For the surface deformations modeled in this investigation, oscillatory behavior does not develop for the single-bump deformations, nor does it appear for the double-bump configuration when the no-slip condition is applied to the plate surface. However, a moderate slip length  $\lambda$ , applied to the double-bump case 2, was found to excite flow features similar to those observed in the earlier investigations. Passaggia *et al.* [3] suggest that the two-dimensional flapping motion varies with the bump height, and the low frequency depends on the precise parameter values. In addition, Dallmann *et al.* [57] conjecture that topological flow changes are responsible for the appearance of unsteady flow or vortex shedding, a view supported by Theofilis *et al.* [58]. Secondary regions of recirculating flow appear near the rear of the primary separation bubble, detach and propagate downstream, with new separation bubbles forming and taking their place. We hypothesize that a similar argument applies to our investigation: oscillatory motion is induced by a combination of surface geometry and topological flow changes. For the case 2 double configuration with a no-slip wall [see Fig. 15(a)], a single, elongated pocket of separated flow forms in the gap between the two bumps, whose amplitude peaks near the gap center. Introducing surface slip reduces the intensity and dimensions of this primary separation bubble. However, surface slip also establishes a second recirculation zone along the rear of the separation bubble and immediately upstream of the second bump. This smaller region of recirculating flow detaches from the primary separation bubble, is swept downstream, and passes over the second bump, leading to the development of oscillatory behavior, as illustrated in Figs. 15(b) and 15(c). In contrast, oscillatory motion is absent from the case 1 double-bump scenario (see Fig. 13). Here, the bumps are located closer together, resulting in a peak in the separation bubble intensity along the front side of the second bump, regardless of the slip length  $\lambda$ . Consequently, secondary regions of recirculating flow fail to manifest. These observations suggest that the distance between neighboring bumps and the location where the separated flow peaks play a crucial role in determining whether self-sustained oscillatory behavior develops. Thus,



similar to [1–3,6,56–58], oscillatory motion depends on the bump dimensions, the distance between adjacent bumps, and topological flow changes.

## VI. CONCLUDING REMARKS

A two-dimensional numerical study has been undertaken on the effect of slip boundary conditions on the flow that develops over small-scale Gaussian-shaped surface deformations on an otherwise flat plate. The Reynolds number of the flow for this study was  $Re = 100\,000$ .

Single, isolated surface deformations were modeled, including bumps and gaps at fixed streamwise  $x$  positions. Results were presented for surface deformations of aspect ratio  $\eta_1$  (i.e., small deformations) and aspect ratio  $\eta_2$  (i.e., large deformations), located at  $x_c = 9$ . In the absence of slip (i.e.,  $\lambda = 0$ ), pockets of separation form along the rear side of the bump and within the gap concavity. Furthermore, bumps establish more intense regions of flow separation than gaps. A slip length  $\lambda = 2.5 \times 10^{-3}$  was sufficient to inhibit separation for the small surface deformations (of aspect ratio  $\eta_1$ ), whereas for the large deformations (of aspect ratio  $\eta_2$ ),  $\lambda = 5 \times 10^{-3}$  and  $\lambda = 7.5 \times 10^{-3}$  were necessary to suppress separation for the bump and gap configurations, respectively.

Subsequently, two double-bump configurations were modeled with bumps of aspect ratio  $\eta_2$  (i.e., large bumps). These configurations were referenced as case 1 and case 2, respectively. In each instance, one bump was located at  $x_c = 9$ , while the other bump was at  $x_c = 8.5$  for case 1 and at  $x_c = 8$  for case 2. The location of the two bumps plays a fundamental role in the evolution of the flow over the double-bump configuration. Two recirculation regions form, one between the two bumps and a second along the rear side of the second bump. For the case 1 double-bump configuration, the separation bubble that forms along the rear side of the second bump was shorter than that which develops for the single-bump arrangement. Thus, the location of the first bump provides a mechanism for flow control. Moreover, a smaller slip length  $\lambda$  was required for the double-bump model than the single-bump configuration to suppress all regions of reversed flow. A slip length  $\lambda = 4 \times 10^{-3}$  inhibits the separation bubble along the rear side of the second bump, and  $\lambda = 6 \times 10^{-3}$  inhibits flow separation in the gap region between the two bumps.

Contrasting behavior emerges for the case 2 double-bump configuration. At moderate slip lengths,  $1.25 \times 10^{-3} \leq \lambda \leq 5 \times 10^{-3}$ , nonlinear oscillatory behavior was generated. This results in pulsating, disconnected pockets of reversed flow that convect downstream and out of the computational domain. Indeed, results were similar to those presented numerically and experimentally by [1–3] on self-sustained low-frequency flapping in a separated flow. Although, notably, unlike earlier studies, the oscillatory phenomenon was not generated for any of the single-bump deformations considered herein. Our results suggest that the geometry (i.e., the height, width, and aspect ratio) of the surface deformations, their relative position, and topological flow changes [57,58] play key roles in establishing oscillatory motion. The biggest oscillations were obtained for  $\lambda = 2.5 \times 10^{-3}$ , while  $\lambda = 7.5 \times 10^{-3}$  was sufficient to eliminate oscillatory behavior and suppress all regions of separated flow.

In future studies, it would be interesting to model the effect of slip on different multibump configurations (i.e., an array of bumps). In addition, an exciting natural extension of this work would be to perform DNS in three dimensions. The flow development over three-dimensional small-scale deformations, with different features (including height, width, location, etc.) may present new characteristics depending on the geometrical configuration and Reynolds number. A series of studies may be undertaken to determine the ideal parameters that convey the quality of a slip surface and establish control of flow separation, laminar flow, turbulent flow, and transition. Preliminary results on the three-dimensional boundary-layer flow over a single-bump deformation, with a no-slip condition on the wall, show that the flow remains laminar for the Reynolds number  $Re = 50\,000$  (i.e., half of that considered in the above two-dimensional investigation). With increased computational resources, DNS for  $Re = 100\,000$  may be realized. We hope to report the results on the effect of slip surfaces on such a flow configuration in the near future.

The authors report no conflict of interest.

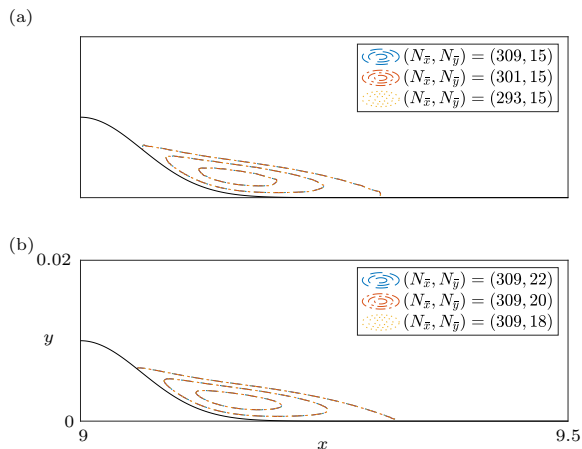


FIG. 20. Contour plots of the streamwise  $u$  velocity in the region of separated flow downstream of the single-bump configuration with aspect ratio,  $\eta_1$ ,  $\Omega_{\bar{x}} = [5, 10]$ , and a no-slip wall, for (a)  $N_{\bar{y}} = 15$  and variable  $N_{\bar{x}}$ , and (b)  $N_{\bar{x}} = 309$  and variable  $N_{\bar{y}}$ .

#### APPENDIX A: GRID RESOLUTION

The accuracy of the solutions presented in this study was confirmed by undertaking a grid resolution analysis, whereby the number of nodes,  $N_{\bar{x}}$  and  $N_{\bar{y}}$ , along the computational  $\bar{x}$  and  $\bar{y}$  directions were varied. Again, utilizing the Nektar++ spectral- $hp$  element method with eighth-order Lagrange polynomials as basis functions, flow past the single-bump of aspect ratio  $\eta_1$  was numerically simulated for several values of  $N_{\bar{x}}$  and  $N_{\bar{y}}$  in the instance the flat plate was subject to the no-slip condition. Figure 20 displays contours of the streamwise  $u$  velocity, specifically the separation bubble that forms downstream of the bump deformation. In Fig. 20(a),  $\Omega_{\bar{x}} = [5, 10]$  and  $N_{\bar{y}} = 15$ , with dashed blue lines representing the solution presented in Figs. 7(a) and 7(b), where  $N_{\bar{x}} = 309$ . The solutions established for a reduced number of  $\bar{x}$  nodes,  $N_{\bar{x}} = 301$  and 293, are given by chain red and dotted yellow lines, respectively. Remarkably, the two sets of contours overlap and exhibit identical minimum values,  $\min(u)$  (see Table IV). Equivalent solutions are plotted in Fig. 20(b), but for the mesh specifications implemented for the large bump of aspect ratio  $\eta_2$ . Namely, the number of  $\bar{y}$  nodes  $N_{\bar{y}} = 22$  (solid blue). In addition, two further cases are displayed, matched to fewer  $\bar{y}$  nodes:  $N_{\bar{y}} = 20$  (chain red) and  $N_{\bar{y}} = 18$  (dotted yellow). Solutions are again identical and in excellent agreement with the results plotted in Fig. 20(a). Hence, when combined with the eighth-order Lagrange polynomial spectral method, the grid specifications implemented in the above study were more than sufficient for accurately capturing the flow dynamics and pockets of separated flow near the surface deformations.

TABLE IV. Minimum of the streamwise  $u$  velocity,  $\min(u)$ , found within the region of separation for the single bump of aspect ratio  $\eta_1$ ,  $\Omega_{\bar{x}} = [5, 10]$ , and grid resolutions modeled in Fig. 20.

$N_{\bar{x}}$	$N_{\bar{y}}$	$\min(u)$
293	15	-0.012207
301	15	-0.012207
309	15	-0.012207
309	18	-0.012274
309	20	-0.012302
309	22	-0.012303

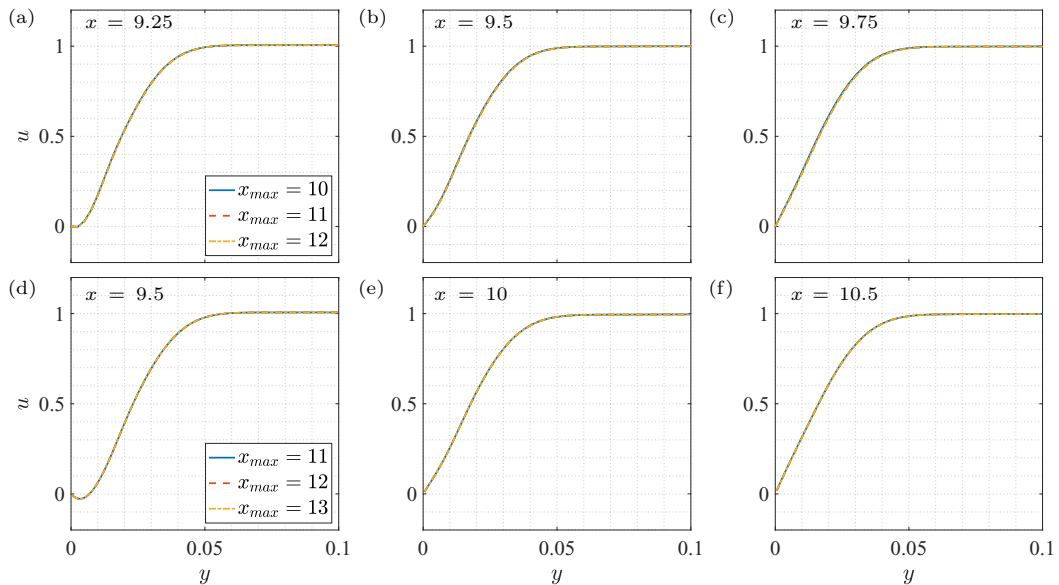


FIG. 21. Streamwise  $u$ -velocity profiles at fixed  $x$  locations for single-bump configurations located at  $x_c = 9$  of aspect ratio (a)–(c)  $\eta_1$  and (d)–(f)  $\eta_2$ . The streamwise location of the outlet in (a)–(c) is  $x_{\max} = 10$  (solid blue lines),  $x_{\max} = 11$  (dashed red), and  $x_{\max} = 12$  (chain yellow), and in (d)–(f) is  $x_{\max} = 11$  (solid blue),  $x_{\max} = 12$  (dashed red), and  $x_{\max} = 13$  (chain yellow).

## APPENDIX B: STREAMWISE LENGTH OF THE COMPUTATIONAL DOMAIN

In the above study, the streamwise length of the computational domain  $\Omega_{\bar{x}} = [5, x_{\max}]$  was chosen to be sufficiently large to avoid interference from the streamwise outlet  $x_{\max}$ , with the flow dynamics that emerged near the surface deformations, and particularly the development of separated flow. In Sec. IV, results were presented for two isolated single-bump deformations of aspect ratio  $\eta_1$  (small bump) and  $\eta_2$  (large bump), located at  $x_c = 9$ , with  $\Omega_{\bar{x}} = [5, 10]$  and  $\Omega_{\bar{x}} = [5, 11]$ , respectively. For each bump deformation, two longer computational domains were modelled to validate the fluid flow behavior downstream of the bump deformity. Figures 21(a)–21(c) compare the velocity profiles obtained for three different computational domains at three successive streamwise  $x$  locations for the small bump. Similarly, Figs. 21(d)–21(f) depict comparable results for the large bump. In each case, there are no discernible differences between the three sets of results.

Figure 22 displays the corresponding distributions of the skin-friction coefficient  $c_f$  for the two single-bump deformations and the three computational domain lengths  $\Omega_{\bar{x}}$ . In both cases, a minor variation in  $c_f$  emerges near the streamwise outlet  $x_{\max}$  of the smaller domains (solid blue lines) compared to the longer domains. However, within the streamwise interval encompassing the bump deformation and flow separation (i.e.,  $c_f < 0$ ), the skin-friction coefficient  $c_f$  is identical. Thus, the shortest computational domains,  $\Omega_{\bar{x}} = [5, 10]$  for the small bump and  $\Omega_{\bar{x}} = [5, 11]$  for the large bump, were sufficient to undertake an accurate computational study of the flow development near the single-bump deformations. Similar conclusions were drawn for the gap and double-bump configurations modeled in this study.

## APPENDIX C: FLOW OVER A LARGER BUMP

In earlier numerical and experimental investigations concerning flow separation along the rear side of a single bump [1–3,6], the bump geometry (i.e., height and width) and flow conditions were sufficient to induce self-sustained nonlinear oscillatory behavior and vortex shedding downstream

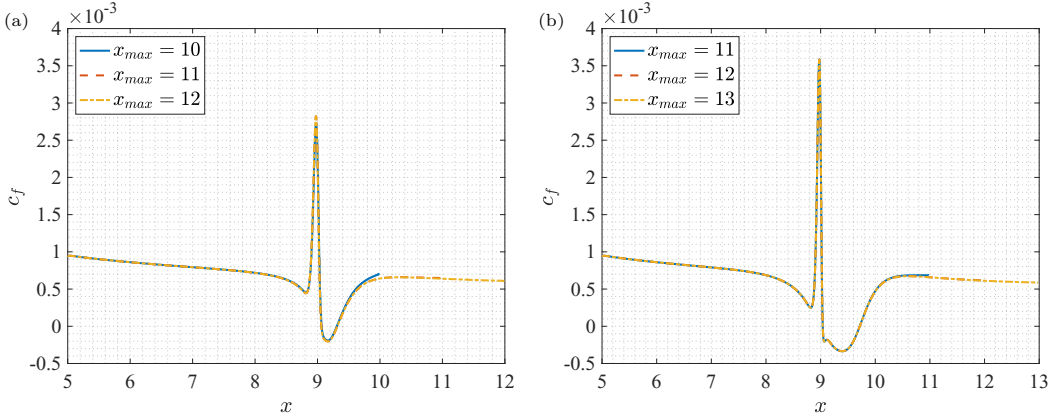


FIG. 22. Distribution of the skin-friction coefficient  $c_f$  for the single-bump configurations (a)  $\eta_1$  and (b)  $\eta_2$  with no-slip walls  $\lambda = 0$  and computational domains of length  $\Omega_{\bar{x}} = [5, x_{\max}]$  and variable streamwise outlet locations  $x_{\max}$ .

of the separation bubble, described as low-frequency flapping, much like that observed for the double-bump configuration case 2. However, for those single-bump configurations modeled in the above study, with aspect ratios  $\eta_1$  and  $\eta_2$ , following a brief transient phase, a steady state was realized, with a singular, elongated separation bubble forming along the rear side of the bump. To test whether the nonlinear oscillatory phenomenon is related to the bump height (and aspect ratio), a third, taller, bump is modeled with height  $h = 0.02$ , width  $\sigma = 0.0625$  (same as bumps  $\eta_1$  and  $\eta_2$ ), and aspect ratio  $\eta = 0.32$  (see the last line in Table I). (Note that this third bump is marginally

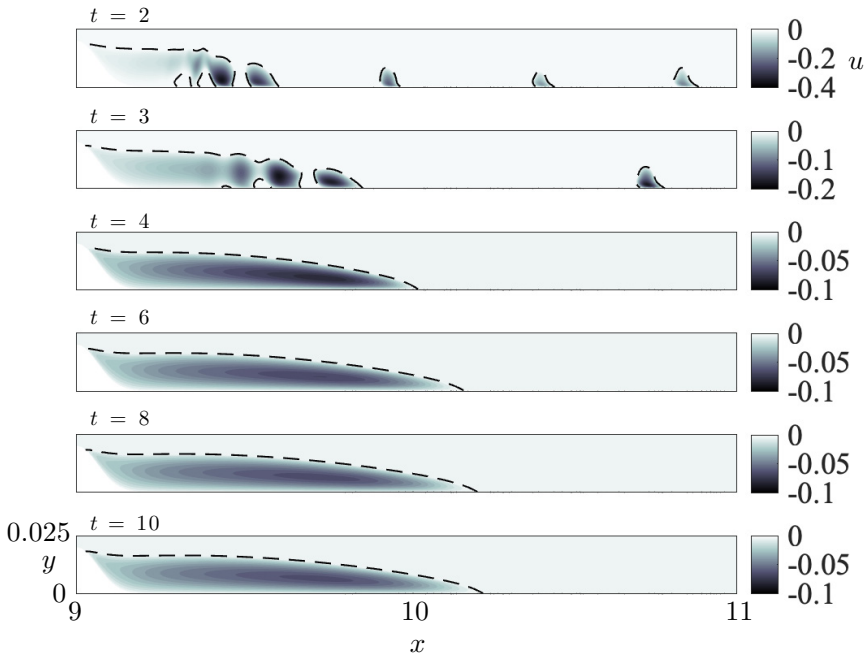


FIG. 23. Contour plots of the streamwise  $u$  velocity in the region of separated flow downstream of the single-bump configuration with aspect ratio  $\eta = 0.32$ , and a no-slip wall, at times  $t = 2, 3, 4, 6, 8$ , and  $10$ . Dashed black lines indicate  $u = 0$ .

smaller than those modeled in [1–3,6].) As before, the streamwise length of the computational domain  $\Omega_{\bar{x}} = [5, x_{\max}]$  was chosen to be sufficiently large to avoid interference with the outlet boundary, with  $x_{\max} = 13$ . Figure 23 exhibits the evolution of the streamwise  $u$  velocity about the separation bubble found downstream of the bump when the wall is subject to the no-slip condition. At time  $t = 2$ , the flow separates along the rear side of the bump with multiple smaller pockets of separated flow shedding from the primary separation bubble. These regions of recirculating flow are swept downstream with a distinct spatial periodicity. However, this behavior does not persist for long, and vortex shedding diminishes. Eventually, a steady state is realized with a single pocket of separated flow established of length  $L \approx 1$ . Thus, the third, taller, bump is again inadequate for generating the self-sustained oscillatory phenomenon. Nevertheless, more pronounced oscillations are observed at early time  $t$  compared to the bump with aspect ratio  $\eta_2$ , depicted in Fig. 4(a). This suggests that further increases in the bump height  $h$  may enhance oscillatory behavior and potentially lead to self-sustained low-frequency flapping akin to [1–3,6].

- 
- [1] M. Marquillie and U. Ehrenstein, On the onset of nonlinear oscillations in a separating boundary-layer flow, *J. Fluid Mech.* **490**, 169 (2003).
  - [2] U. Ehrenstein and F. Gallaire, Two-dimensional global low-frequency oscillations in a separating boundary-layer flow, *J. Fluid Mech.* **614**, 315 (2008).
  - [3] P.-Y. Passaggia, T. Leweke, and U. Ehrenstein, Transverse instability and low-frequency flapping in incompressible separated boundary layer flows: an experimental study, *J. Fluid Mech.* **703**, 363 (2012).
  - [4] P. Huerre and P. A. Monkewitz, Local and global instabilities in spatially developing flows, *Annu. Rev. Fluid Mech.* **22**, 473 (1990).
  - [5] J.-M. Chomaz, Global instabilities in spatially developing flows: Non-normality and nonlinearity, *Annu. Rev. Fluid Mech.* **37**, 357 (2005).
  - [6] P.-Y. Passaggia and U. Ehrenstein, Optimal control of a separated boundary-layer flow over a bump, *J. Fluid Mech.* **840**, 238 (2018).
  - [7] M. Gad-el-Hak, Modern developments in flow control, *Appl. Mech. Rev.* **49**, 365 (1996).
  - [8] P. R. Ashill, J. L. Fulker, and K. C. Hackett, A review of recent developments in flow control, *Aeronaut. J.* **109**, 205 (2005).
  - [9] P. Thompson and S. Troian, A general boundary condition for liquid flow at solid surfaces, *Nature (London)* **389**, 360 (1997).
  - [10] D. Legendre, E. Lauga, and J. Magnaudet, Influence of slip on the dynamics of two-dimensional wakes, *J. Fluid Mech.* **633**, 437 (2009).
  - [11] C. Wang and M. Gharib, Effect of the dynamic slip boundary condition on the near-wall turbulent boundary layer, *J. Fluid Mech.* **901**, A11 (2020).
  - [12] N. Beratlis, E. Balaras, and K. Squires, The role of surface texturing on the physics of boundary layer separation over a bump, *Int. J. Heat Fluid Flow* **73**, 223 (2018).
  - [13] S. Parvate, P. Dixit, and S. Chattopadhyay, Superhydrophobic surfaces: Insights from theory and experiment, *J. Phys. Chem. B* **124**, 1323 (2020).
  - [14] Y. Bai, H. Zhang, Y. Shao, H. Zhang, and J. Zhu, Recent progresses of superhydrophobic coatings in different application fields: An overview, *Coatings* **11**, 116 (2021).
  - [15] K. Fukuda, J. Tokunaga, T. Nobunaga, T. Nakatani, T. Iwasaki, and Y. Kunitake, Frictional drag reduction with air lubricant over a super-water-repellent surface, *J. Mar. Sci. Technol.* **5**, 123 (2000).
  - [16] J. P. Rothstein, Slip on superhydrophobic surfaces, *Annu. Rev. Fluid Mech.* **42**, 89 (2010).
  - [17] K. B. Golovin, J. W. Gose, M. Perlin, S. L. Ceccio, and A. Tuteja, Bioinspired surfaces for turbulent drag reduction, *Philos. Trans. R. Soc. A* **374**, 20160189 (2016).
  - [18] N. Miljkovic and E. N. Wang, Condensation heat transfer on superhydrophobic surfaces, *MRS Bull.* **38**, 397 (2013).

- [19] T. Verho, C. Bower, P. Andrew, S. Franssila, O. Ikkala, and R. Ras, Mechanically durable superhydrophobic surfaces, *Adv. Mater.* **23**, 673 (2011).
- [20] J. Seo, R. García-Mayoral, and A. Mani, Pressure fluctuations and interfacial robustness in turbulent flows over superhydrophobic surfaces, *J. Fluid Mech.* **783**, 448 (2015).
- [21] R. García-Mayoral and J. Jiménez, Hydrodynamic stability and breakdown of the viscous regime over riblets, *J. Fluid Mech.* **678**, 317 (2011).
- [22] S. Endrikat, D. Modesti, M. MacDonald, R. García-Mayoral, N. Hutchins, and D. Chung, Direct numerical simulations of turbulent flow over various riblet shapes in minimal-span channels, *Flow, Turbul. Combust.* **107**, 1 (2021).
- [23] S. Türk, G. Daschiel, A. Stroh, Y. Hasegawa, and B. Frohnäpfel, Turbulent flow over superhydrophobic surfaces with streamwise grooves, *J. Fluid Mech.* **747**, 186 (2014).
- [24] C. T. Fairhall, N. Abderrahaman-Elena, and R. García-Mayoral, The effect of slip and surface texture on turbulence over superhydrophobic surfaces, *J. Fluid Mech.* **861**, 88 (2019).
- [25] J. I. Ibrahim, G. Gómez-de Segura, D. Chung, and R. García-Mayoral, The smooth-wall-like behaviour of turbulence over drag-altering surfaces: a unifying virtual-origin framework, *J. Fluid Mech.* **915**, A56 (2021).
- [26] N. Abderrahaman-Elena, C. T. Fairhall, and R. García-Mayoral, Modulation of near-wall turbulence in the transitionally rough regime, *J. Fluid Mech.* **865**, 1042 (2019).
- [27] F. Picella, J.-C. Robinet, and S. Cherubini, On the influence of the modelling of superhydrophobic surfaces on laminar-turbulent transition, *J. Fluid Mech.* **901**, A15 (2020).
- [28] J.-P. Mollicone, F. Battista, P. Gualtieri, and C. M. Casciola, Effect of geometry and Reynolds number on the turbulent separated flow behind a bulge in a channel, *J. Fluid Mech.* **823**, 100 (2017).
- [29] S. Ceccacci, S. A. W. Calabretto, C. Thomas, and J. P. Denier, The effect of slip on the development of flow separation due to a bump in a channel, *J. Fluid Mech.* **951**, A31 (2022).
- [30] A. Niavarani and N. V. Priezjev, The effective slip length and vortex formation in laminar flow over a rough surface, *Phys. Fluids* **21**, 052105 (2009).
- [31] N. V. Priezjev and S. M. Troian, Influence of periodic wall roughness on the slip behaviour at liquid/solid interfaces: molecular-scale simulations versus continuum predictions, *J. Fluid Mech.* **554**, 25 (2006).
- [32] O. G. Akinlade and D. J. Bergstrom, Effect of surface roughness on the coefficients of a power law for the mean velocity in a turbulent boundary layer, *J. Turbul.* **8**, N18 (2007).
- [33] S. Song and J. Eaton, The effects of wall roughness on the separated flow over a smoothly contoured ramp, *Exp. Fluids* **33**, 38 (2002).
- [34] C. Liu, Y. Li, Z. Zhou, and P. Wiśniewski, Effect of cascade surface roughness on boundary layer flow under variable conditions, *Front. Energy Res.* **9**, 818828 (2022).
- [35] C. D. Aubertine, J. K. Eaton, and S. Song, Parameters controlling roughness effects in a separating boundary layer, *Int. J. Heat Fluid Flow* **25**, 444 (2004).
- [36] C. L. M. H. Navier, Mémoire sur les lois du mouvement des fluides, *Mem. Acad. Sci. Inst. Fr.* **6**, 389 (1823).
- [37] T. Min and J. Kim, Effects of hydrophobic surface on skin-friction drag, *Phys. Fluids* **16**, L55 (2004).
- [38] S. Ceccacci, S. A. W. Calabretto, C. Thomas, and J. P. Denier, The linear stability of slip channel flows, *Phys. Fluids* **34**, 074103 (2022).
- [39] A. Busse and N. D. Sandham, Influence of an anisotropic slip-length boundary condition on turbulent channel flow, *Phys. Fluids* **24**, 055111 (2012).
- [40] C. T. Fairhall and R. García-Mayoral, Spectral analysis of the slip-length model for turbulence over textured superhydrophobic surfaces, *Flow, Turbul. Combust.* **100**, 961 (2018).
- [41] B. Mele and R. Tognaccini, Slip length based boundary condition for modeling drag reduction devices, *AIAA J.* **56**, 3478 (2018).
- [42] J. O. Pralits, E. Alinovi, and A. Bottaro, Stability of the flow in a plane microchannel with one or two superhydrophobic walls, *Phys. Rev. Fluids* **2**, 013901 (2017).
- [43] D. W. Bechert, M. Bruse, W. Hage, J. G. T. Van Der Hoeven, and G. Hoppe, Experiments on drag-reducing surfaces and their optimization with an adjustable geometry, *J. Fluid Mech.* **338**, 59 (1997).

- [44] D. W. Bechert and M. Bartenwerfer, The viscous flow on surfaces with longitudinal ribs, *J. Fluid Mech.* **206**, 105 (1989).
- [45] P. Luchini, F. Manzo, and A. Pozzi, Resistance of a grooved surface to parallel flow and cross-flow, *J. Fluid Mech.* **228**, 87 (1991).
- [46] H. Xu, S. J. Sherwin, P. Hall, and X. Wu, The behaviour of Tollmien–Schlichting waves undergoing small-scale localised distortions, *J. Fluid Mech.* **792**, 499 (2016).
- [47] D. Serson, J. R. Meneghini, and S. J. Sherwin, Velocity-correction schemes for the incompressible Navier–Stokes equations in general coordinate systems, *J. Comput. Phys.* **316**, 243 (2016).
- [48] C. D. Cantwell, D. Moxey, A. Comerford, A. Bolis, G. Rocco, G. Mengaldo, D. De Grazia, S. Yakovlev, J. E. Lombard, D. Ekelschot, B. Jordi, H. Xu, Y. Mohamied, C. Eskilsson, B. Nelson, P. Vos, C. Biotto, R. M. Kirby, and S. J. Sherwin, Nektar + +: An open-source spectral/hp element framework, *Comput. Phys. Commun.* **192**, 205 (2015).
- [49] S. Dong, A convective-like energy-stable open boundary condition for simulations of incompressible flows, *J. Comput. Phys.* **302**, 300 (2015).
- [50] S. Ceccacci, Control of boundary-layer separation using surface roughness, Ph.D. thesis, Macquarie University, Sydney, 2023.
- [51] C. Geuzaine and J.-F. Remacle, Gmsh: A 3-D finite element mesh generator with built-in pre- and post-processing facilities, *Int. J. Num. Methods Eng.* **79**, 1309 (2009).
- [52] Y.-S. Wie and M. R. Malik, Effect of surface waviness on boundary-layer transition in two-dimensional flow, *Comput. Fluids* **27**, 157 (1998).
- [53] C. Thomas, S. Mughal, and R. Ashworth, Development of Tollmien–Schlichting disturbances in the presence of laminar separation bubbles on an unswept infinite wavy wing, *Phys. Rev. Fluids* **2**, 043903 (2017).
- [54] J. Banchetti, P. Luchini, and M. Quadrio, Turbulent drag reduction over curved walls, *J. Fluid Mech.* **896**, A10 (2020).
- [55] J.-P. Mollicone, F. Battista, P. Gualtieri, and C. M. Casciola, Superhydrophobic surfaces to reduce form drag in turbulent separated flows, *AIP Adv.* **12**, 075003 (2022).
- [56] S. N. Sinha, A. K. Gupta, and M. M. Oberai, Laminar separating flow over backsteps and cavities. I - Backsteps, *AIAA J.* **19**, 1527 (1981).
- [57] U. Dallmann, T. Herberg, H. Gebing, W.-H. Su, and H.-Q. Zhang, Flow field diagnostics: Topological flow changes and spatio-temporal flow structure, *AIAA Paper 95-0791* (1995).
- [58] V. Theofilis, S. Hein, and U. Dallmann, On the origins of unsteadiness and three-dimensionality in a laminar separation bubble, *Philos. Trans. R. Soc. London A* **358**, 3229 (2000).